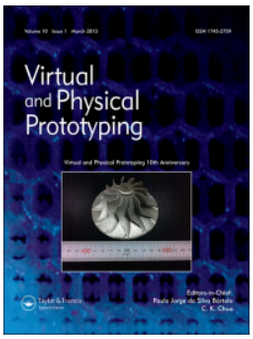

Virtual and Physical Prototyping

ISSN: 1745-2759 (Print) 1745-2767 (Online) Journal homepage: www.tandfonline.com/journals/nvpp20

A novel bypass-gas metal arc directed energy deposition for in-situ synthesis Al–Cu–Li alloy: exploring the microstructure and mechanical properties evolution from as-deposited state to T6 state

Fenglei Cao, Dianlong Wang, Yunfei Gu, Jiajia Shen, Ziwei Bai, Zhen Tan, Zhimin Liang, Zhenzhen Peng, Xiao Yang, Shaohui Chen, Zhi Zeng, Liwei Wang & J. P. Oliveira

To cite this article: Fenglei Cao, Dianlong Wang, Yunfei Gu, Jiajia Shen, Ziwei Bai, Zhen Tan, Zhimin Liang, Zhenzhen Peng, Xiao Yang, Shaohui Chen, Zhi Zeng, Liwei Wang & J. P. Oliveira (2025) A novel bypass-gas metal arc directed energy deposition for in-situ synthesis Al–Cu–Li alloy: exploring the microstructure and mechanical properties evolution from as-deposited state to T6 state, Virtual and Physical Prototyping, 20:1, e2472394, DOI: 10.1080/17452759.2025.2472394

To link to this article: https://doi.org/10.1080/17452759.2025.2472394

Published online: 19 Mar 2025.

VIRTUAL AND PHYSICAL PROTOTYPING
2025, VOL. 20, NO. 1, e2472394 (22 pages)
https://doi.org/10.1080/17452759.2025.2472394

A novel bypass-gas metal arc directed energy deposition for in-situ synthesis Al–Cu–Li alloy: exploring the microstructure and mechanical properties evolution from as-deposited state to T6 state

Fenglei Cao[a]*, Dianlong Wang[b]*, Yunfei Gu[a], Jiajia Shen[e], Ziwei Bai[a], Zhen Tan[a], Zhimin Liang[a], Zhenzhen Peng[a], Xiao Yang[a], Shaohui Chen[c], Zhi Zeng[d], Liwei Wang[a] and J. P. Oliveira [e]

[a]Hebei Key Laboratory of Material Near-Net Forming Technology, School of Materials Science and Engineering, Hebei University of Science and Technology, Shijiazhuang, People's Republic of China; [b]School of Mechanical Engineering, Yanshan University, Qinhuangdao, People's Republic of China; [c]Beijing Aeronautical Technology Research Center, Beijing, People's Republic of China; [d]School of Mechanical and Electrical Engineering, University of Electronic Science and Technology, Chengdu, People's Republic of China; [e]CENIMAT/I3N, Department of Materials Science, NOVA School of Science and Technology, Universidade NOVA de Lisboa, Caparica, Portugal

ABSTRACT

A novel bypass-gas metal arc directed energy deposition (bypass-GMA DED) was proposed to prepare high strength Al–Cu–Li-based components. An Al–5.51Cu–0.48Li alloy was successfully prepared, followed by subsequent T6 treatment. The microstructure evolution and improvement of mechanical properties after the T6 state were benchmarked against the as-deposited condition. The component fabricated by bypass-GMA DED has obvious periodic distribution characteristics, with a large number of fine equiaxed grains distributed near the interlayer fusion boundary and coarse columnar grains within the intralayer region. After heat treatment, the Al–5.51Cu–0.48Li alloy is mainly composed of four types of strengthening phases, θ', θ'', δ' and T_1, which contrasts with the sole presence of θ phase in the deposited condition. These phases are conducive to the improvement of mechanical properties. The strength of the prepared alloy is higher than those additively manufactured Al–Cu–Li alloys, reaching values similar to those of conventional third generation Al–Cu–Li alloys.

ARTICLE HISTORY
Received 8 November 2024
Accepted 21 February 2025

KEYWORDS
Bypass-gas metal arc directed energy deposition (bypass-GMA DED); Al–Cu–Li alloy; intermediate alloys; microstructure; mechanical properties

1. Introduction

Due to the need to reduce structural weight and improving stiffness, Al–Cu–Li alloys have become the preferred material to achieve weight savings and performance improvements in the manufacturing of various modern aircrafts [1,2]. So, these alloys are widely used in the preparation of aviation and aerospace structural parts instead of conventional Al alloys. For the existing manufacturing technologies for the fabrication of complex structures, there are disadvantages such as difficult operation, long moulding cycle and often complicated thermomechanical processing [3]. Moreover, conventionally fabricated structural parts will have a significant material waste problem. Therefore, new processing methods suitable for the fabrication of Al–Cu–Li structural alloys with less material waste and flexible manufacturing are urgently needed. In recent years, additive manufacturing (AM) has been shown to possess the advantages of high forming efficiency, high material utilisation rate and high flexibility [4], making it possible to manufacture complex structural parts in a cost-effective way. At present, metallic AM usually uses lasers, electron beams or electric arcs as heat sources, and the raw material is fed in the form of powder or wire.

Although Al–Li alloys have some potential applications in laser additive manufacturing such as laser powder bed fusion (LPBF) and laser metal deposition (LMD), they still face a number of challenges. First, Li and Mg are prone to burning at high temperatures, which affects the stability of alloy composition. Xu et al. [5] prepared Al–4Cu–1Li–0.4Mg–0.5Zr alloys by LPBF using pure Cu, Al, Mg powder and Al–5Li, Al–7.04Zr alloys as raw materials. In addition, craters, porosity and cracks on the prepared components were observed, suggesting that LPBF may not be suitable for the fabrication of Al–Li alloys. Second, due to the

CONTACT J. P. Oliveira jp.oliveira@fct.unl.pt CENIMAT/I3N, Department of Materials Science, NOVA School of Science and Technology, Universidade NOVA de Lisboa, Caparica 2829-516, Portugal; Liwei Wang wangliwei110127@163.com Hebei Key Laboratory of Material Near-Net Forming Technology, School of Materials Science and Engineering, Hebei University of Science and Technology, Shijiazhuang 050018, People's Republic of China
*The author's total contribution to this work.

influence of temperature gradient and cooling rate in laser additive manufacturing, the phase transformation behaviour and microstructure of different regions along the height are different, which affects the uniformity (microstructure and mechanical) of the components. Jiao et al. [6] prepared a thin-walled 2A97 Al–Li alloy by LMD, and the microstructure of the deposited Al–Li alloy was different along the height of the material, and the top was mainly composed of α (Al) matrix, and the Cu-rich phase was distributed at the grain boundary. The volume fraction of T_B (Al_7Cu_4Li) phases and needle-like T_B (Al_7Cu_4Li) and T_1 (Al_2CuLi) minority phases decreases from bottom to top of the material. The results show that the laser additive manufacturing of Al–Li alloys will render the development of an uneven structure in the as-deposited conditions. Third, during laser additive manufacturing, the diffusion of Al–Li powder is poor, which, compounded by its low density and poor fluidity, makes it is easy to produce metallurgical defects and forming problems, ultimately leading to poor mechanical properties. For example, the tensile strength of the Al–Li alloy components prepared by Wang et al. [7] only reached 458 MPa after heat treatment, mainly because of the large number of metallurgical defects in the components.

Additive friction stir deposition (AFSD) has the advantages of high material utilisation rate and low processing temperature, but it has problems such as low process maturity, and the prepared components have limited shape design and mechanical properties [8,9]. Li et al. [10] used an AFSD system to deposit 2195 Al–Li alloy components with a length of 100 mm. The ultimate tensile strength of the Al–Li alloy after T6 heat treatment reached 505 MPa.

Compared to other AM methods (LPBF, LMD, and AFSD), wire and arc additive manufacturing (WAAM) is more capable of manufacturing large-size structural parts [11]. It can also greatly reduce the material removal rate, reducing manufacturing costs and production cycles. However, WAAM of Al–Cu–Li alloy still faces two problems: (i) the lower mechanical properties of the as-built parts. (ii) customised Al–Cu–Li wires are only fabricated at a laboratory scale. Because of its high strength and low elongation, Al–Cu–Li alloys are usually difficult to form continuous filaments to produce wires. Meanwhile, AM-fabricated components often impose strict requirements for the uniformity of composition, consistency of diameter, and surface quality of the feeding wires. Zhong et al. [12] and Xue et al. [13] respectively prepared 2050Al–Li and AA2196Al–Li alloy straight-walled walls by WAAM using customised Al–Li welding wire as raw materials. After T6 heat treatment, the ultimate tensile strength of the components reached 400 and 439 MPa, respectively.

In summary, although AM has outstanding advantages in terms of efficient forming, material utilisation, and flexibility, the Al–Cu–Li AM alloys still faces challenges such as difficult preparation of raw materials, uneven microstructure, and low mechanical properties [14]. In this paper, aiming at solving the problems of low strength of WAAMed Al–Cu–Li alloys compounded by the difficult preparation of wire feedstock, a bypass-gas metal arc directed energy deposition (bypass-GMA DED) system was proposed for in-situ synthesis Al–Cu–Li alloys. Bypass-GMA DED can reduce heat loss to materials and metallurgical defects such as cracks and porosity caused by incomplete melting or excessive heat input. At the same time, it can provide better temperature control and reduce the temperature gradient during the forming process, thereby improving the microstructure uniformity of the material and improving the mechanical properties. At present, the Bypass-GMA DED technology has the advantage of flexible raw material selection, and has been used to synthesise Al–Mg–Cu alloys [15], 2024 alloys [16], and Al–Zn–Mg–Cu alloys [17,18], but the mechanical properties of the alloys need to be further improved. Therefore, in this study, the main welding wire of the bypass-GMA DED system was the Al–Cu wire, and the bypass tape was the Al–Li alloy. The microstructure evolution and mechanical properties of before and after T6 heat treatment were evaluated. This research has significant practical significance and application potential of high strength AMed Al–Cu–Li alloys.

2. Material and methods

In this study, the developed bypass-GMA DED system composed of a Fronius welding power source, a KUKA robot and a bypass intermediate alloy feeding mechanism. Figure 1 shows a schematic of the process. An ER 2319 welding wire with the diameter of 1.2 mm is used as the main wire (middle position), and a strip-shaped 2A97 intermediate alloy with the size of 250 mm × 2 mm × 2 mm produced by Zhengzhou Qingyan Technology Co., LTD was also selected. The density of the intermediate alloy 2A97 and 2319 wire is 2.7 and 2.71g/cm^3, respectively. The angle between the intermediate alloy and the main wire was set to 60°. A 5083 Al alloy plate measuring 350 mm × 150 mm × 10 mm was used as the substrate. The chemical compositions of welding wire, intermediate alloy and substrate are shown in Table 1. Before AM, the oxide film and impurities on the surface of the substrate and intermediate alloy are removed by grinding and acetone

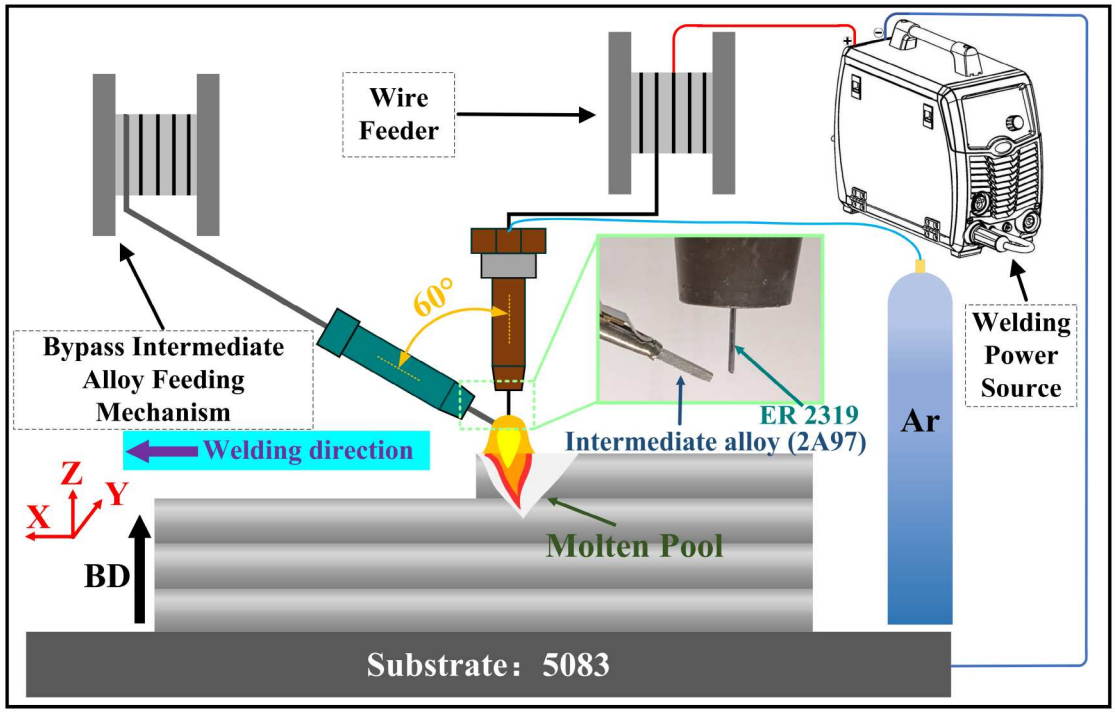

Figure 1. Schematic representation of the developed bypass-GMA DED process.

cleaning. During the process, argon gas with a concentration of 99.999% is used as the shielding gas, and the gas flow rate is set at 20 L/min. The position of the substrate is fixed, and the moving speed of the welding torch is 0.5 m/min. The waiting time between layers is 120 s, to ensure that the temperature of the previous layer is lower than 100°C when the next deposition is made. The specific additive manufacturing parameters of 2319 and Al–Cu–Li alloys are shown in Table 2. The role of T6 heat treatment on the fabricated material was also assessed. For this comparison of microstructure and properties between the as-deposited and T6 condition materials was performed as detailed next.

Figure 2 details the location from where samples for characterisation were taken. Characterisation of the microstructure encompassed, light optical microscopy (OM), scanning and transmission electron microscopy (SEM/TEM), the former aided by electron backscattered diffraction (EBSD).

Inductively coupled plasma atomic emission spectroscopy (ICP-AES, Horiba Ultima2) was used to determine the chemical composition of the fabricated materials. Samples used for microstructure characterisation were polished and then Keller's solution was used to reveal the grain structure features. Phase identification was by X-ray diffraction using a D/MAX-2500 X-ray diffractometer.

Further, the mechanical properties of the fabricated parts were evaluated combining both microhardness and tensile testing. Microhardness testing was performed using a load of 500 gf. Tensile testing was performed at a cross-head speed rate of 0.5 mm/min and strain rate of 6×10^{-4} s^{-1} at room temperature. 3 samples obtained in the longitudinal (parallel to the BD) and transverse (perpendicular to the BD) directions were tested respectively.

3. Results and discussion

3.1. Chemical composition and microstructure of the fabricated parts

According to the feed speed, wire feeding time, wire density and the proportion of elements in the 2319 wire and the intermediate alloy 2A97, the mass percentages (wt.%) of Li and Cu elements in the fabricated components can be calculated as $\omega(Li) = (0.50 \sim 0.62)wt\%$ and $\omega(Cu) = (4.99 \sim 5.72)wt\%$, as shown in Table 3.

The elemental composition of the bypass-GMA DED Al–Cu–Li alloy was also measured by ICP-AES (Table 3). In this part, the proportion of Li (0.48 wt.%) is below that of the theoretical proportion due to burning losses during the process. The proportion of Cu was measured to be 5.51 wt.%. It can be found that the actual measured elemental content is consistent with the theoretical calculation from Table 3. This suggests a high stability of the bypass-GMA DED process. It is generally believed that when the mass percentage of Li and

Table 1. Chemical composition of welding wire, intermediate alloy and substrate.

	Chemical composition. (wt.%)									
Alloys	Cu	Li	Mg	Zn	Mn	Si	Ti	Fe	Zr	Al
ER 2319	5.8–6.8	/	0.02	0.1	0.2–0.4	0.25	/	/	/	Bal
Intermediate alloy 2A97	3.7–4.0	1.3–1.6	0.35–0.55	0.4–0.6	0.31	0.04	0.02	0.02	0.1–0.2	Bal
5083	0.07	/	3.75	0.04	0.49	0.09	/	0.2	/	Bal

Cu in Al–Cu–Li alloy reaches < 2.0 wt.% and > 2.5 wt.%, respectively, the alloy will belong to the third generation Al–Cu–Li alloys. Moreover, the high Cu/Li ratio (11.5) of the fabricated alloy is also in line with the development trend of Al–Cu–Li alloys. Thus, this innovative approach allowed to develop a third generation Al–Cu–Li alloy, with an increase in Cu content and decrease in Li, and the increase of the Cu/Li ration promotes a strengthening effect which can positively impact the mechanical properties of the fabricated material [19].

Figure 3 depicts the macroscopic morphology of the cross section of the bypass-GMA DED Al–5.51Cu–0.48Li alloy component. The component shows that no cracks developed, but a small number of pores appear inside the component. Figure 3(a,c,e) correspond to the interlayer regions at the top, middle and bottom of the component respectively, and Figure 3(b,d,f) are the layer central regions at the top, middle and bottom of the component respectively. Fine equiaxed grains (white arrow) are distributed around the fusion line (dotted green line), while pores in the component are mainly distributed along the fusion line, and the intralayer is mainly composed by coarse columnar grains (yellow arrow). It can be seen from Figure 3(a,c,e) that there are more fine equiaxed grains near the fusion line at the bottom, which is caused by the heat from the upper layer heating the lower layer (causing an intrinsic heat treatment) during the bypass-GMA DED process, resulting in recrystallisation near the fusion line at the bottom. It can be seen from Figure 3(b,d,f) that the columnar grains mainly grow along the BD, and the dendritic segregation occurs inside the coarse columnar grains. Different grain structures appear in different regions, which are caused by factors such as temperature field, cooling rate, solidification process, etc. In the middle of the deposited layer, the temperature of the melt pool is higher due to the higher heat input and slower cooling rate. As the molten pool cools, the solidification process of the liquid phase is relatively slow, and the metal grains grow along the direction of heat flow under the influence of the temperature field, resulting in the formation of coarse columnar crystals. In the interlayer region of the deposited layer, the cooling rate is faster when the new layer of molten pool comes into contact with the lower layer, as each layer is already cooled with a cooler solid metal underneath. The high cooling rate promotes rapid solidification, which leads to the formation of fine equiaxed crystals.

The distribution of the grain structure greatly affects the mechanical properties of the alloy, and coarse columnar grains often result in lower mechanical properties, especially in terms of tensile and fatigue. The growth direction of columnar crystals is usually along the temperature gradient, and the grain boundaries are relatively concentrated and inhomogeneous, resulting in a large slip resistance at the grain boundaries, which limits the plastic deformation ability of the material. The structure of fine equiaxed grains can often significantly improve the mechanical properties of materials, especially in terms of tensile strength and plasticity. As the number of grain boundaries increases by the fine grains, the inhibitory effect of grain boundaries on plastic deformation is enhanced, which significantly increases the strength of the material.

A small number of porosity defects appear in Figure 3, which are usually caused by the dissolution and incomplete escape of gases in the molten pool. Porosity has a negative impact on the mechanical properties of alloys, especially in terms of strength, plasticity, and fracture behaviour. During additive manufacturing of aluminium alloys, the development of porosity is a common defect, and no additive manufacturing technology can completely avoid the formation of porosity, similar to what occurs during casting. Therefore, it is necessary to strictly control/optimise the process parameters and develop subsequent heat treatment to reduce the negative

Table 2. Specific additive manufacturing parameters of 2319 and Al–Cu–Li alloys.

Additive manufacturing parameters	Density (g/cm^3)	Current (A)	Deposition speed (m/min)	Feeding speed (m/min)		Interlayer waiting time (s)	Gas flow speed (L/min)
				ER2319	2A97		
2319 alloy	2.71	120	0.50	5.30	/	120	20
Al–Cu–Li alloy	2.7	120	0.50	5.30	0.95	120	20

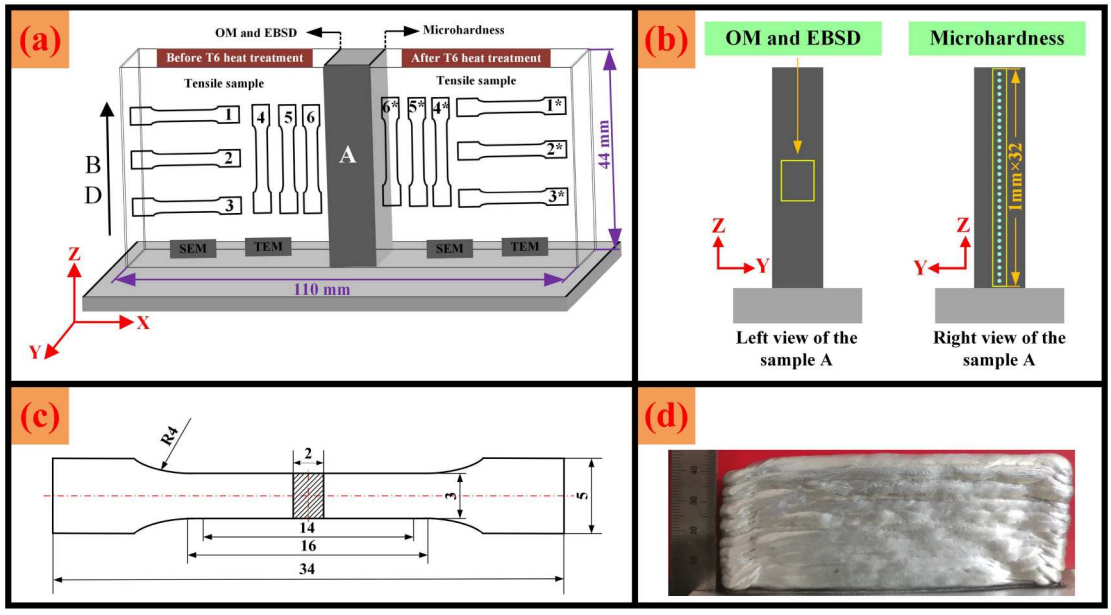

Figure 2. Schematic representation of samples used for microstructure and mechanical characterisation: (a) position of the samples used for characterisation, (b) location analysis for OM, EBSD and micro-hardness testing, (c) tensile sample dimensions, (d) appearance of fabricated part (unit: mm).

impact of pores on the mechanical properties of components.

The grain morphology and texture of the prepared Al–5.51Cu–0.48Li alloy components by bypass-GMA DED were analysed by EBSD in the YZ section. Analysis was performed into interlayer and interlayer centre region. In Figure 4, regions B and C correspond to the top deposited layer, regions D and E are selected from the middle-deposited layer, while regions F and G correspond to the bottom deposited layer. Regions B, D and F are from central regions of each layer, and regions C, E and G were obtained from the interlayer regions. As shown in Figure 4(d–i), different IPF colours represent different directions. Because the sample was deposited layer by layer manner, its macro structure showed typical layered characteristics. As shown in Figure 4(d–i), the fusion lines (marked with black dotted lines) are clearly visible in the interlayer region (Figure 4(e,g,i)), and columnar and equiaxed grain structures are found to exist on the upper and lower sides of the fusion line, respectively. Concerning the central part of the top layer, the grain structure shown in Figure 4(d,f) exhibits a grain structure featuring columnar grains. The fusion line is located between the fine equiaxed grains and the cellular grains, and remelting occurs in part of the interlayer due to heat input of the next layer to be deposited. Equiaxed grains form due to partial melting in subsequent layers and are typically found at the boundary of columnar grains because of the local solidification conditions [20]. Therefore, the coarse grains in the unmelted area below the fusion line result from repeated heat input associated to the process [21]. The grain distribution is due to the blocking and growth of certain grains during deposition and remelting. The stable arc heat input of the molten pool and the relatively low rate of thermal decomposition create an environment conducive to the growth of columnar grains. Consequently, the microstructure of the components produced by bypass-GMA DED is not formed in a single step but evolved due to multiple remelting and heat treatment cycles. When the (N + 1) layer remelts the N layer, the arc heats the (N–1) layer. Dong et al. [22] reported that a single deposited layer was divided into upper and lower parts by the conventional WAAM process. Due to the low heat input of the cold metal transfer (CMT) process, bypass-GMA DED has no obvious signs of stratification, and the grain distribution is more uniform which is expected to confer a more isotropic behaviour.

Compared to the top and middle layers, the grain morphology and texture of the bottom layer are slightly different. Figure 4(j) and (k), (l) and (m), (n) and (o) details the grain size statistics for the top layer centre and interlayer, middle layer centre and interlayer, bottom layer centre and interlayer. The average grain size difference between the top, middle and bottom layers is 47.8%, 42.2% and 67.5%, respectively. The reason for these grain size difference can be attributed to heat accumulation and remelting. The heat accumulation induced by the electric arc makes the cooling rate of the top layer to decrease, which promote grain growth.

Table 3. Practical and theoretical proportions of each element in bypass-GMA DED Al–Cu–Li alloy part.

Alloy		Chemical composition (wt.%)							
		Cu	Li	Mg	Zn	Mn	Ti	Fe	Zr
Bypass-GMA DED Al–Cu–Li alloy	ICP-AES measurement	5.51	0.48	0.18	0.26	0.29	0.08	0.21	0.15
	Theoretical calculation	4.99–5.72	0.50–0.62	/	/	/	/	/	/

Figure 4(p) and (q), (r) and (s), (t) and (u) depict the pole figures of the top, middle and bottom layers of YZ section of the Al–5.51Cu–0.48Li component, respectively. The maximum texture index reaching 8.208 and 4.323, 8.272 and 2.837, and 4.033 and 1.223, respectively. The maximum texture index of the Al–5.51Cu–0.48Li components is large in the intralayer region, and small in the interlayer region, indicating that the grain texture characteristics vary within the deposited material. In fact, the intralayer region is mainly composed coarse columnar grains, and there are more fine equiaxed grains in the interlayer region, which is consistent with the results in Figure 4(d–i), reflecting the effects of heat input and remelting on the grain texture development during the deposition process.

In addition, the texture of the deposited alloy shows a pronounced [100] texture along the deposition direction. This is because in the bypass-GMA DED process, where the heat input to the melt pool, the cooling conditions, and the grain growth mechanism determine the preferential orientation of a particular crystal orientations during deposition. Al alloys have a face-centred cubic (FCC) crystal structure, and the [100] direction usually has a lower surface energy and a higher crystal growth rate, so it is easy for grains preferentially to preferentially grow along the [100] direction during deposition. Changes in heat input affect the direction of grain growth and texture formation. At higher heat inputs, grains usually solidify and grow in directions in easy grow directions. Under rapid cooling and local

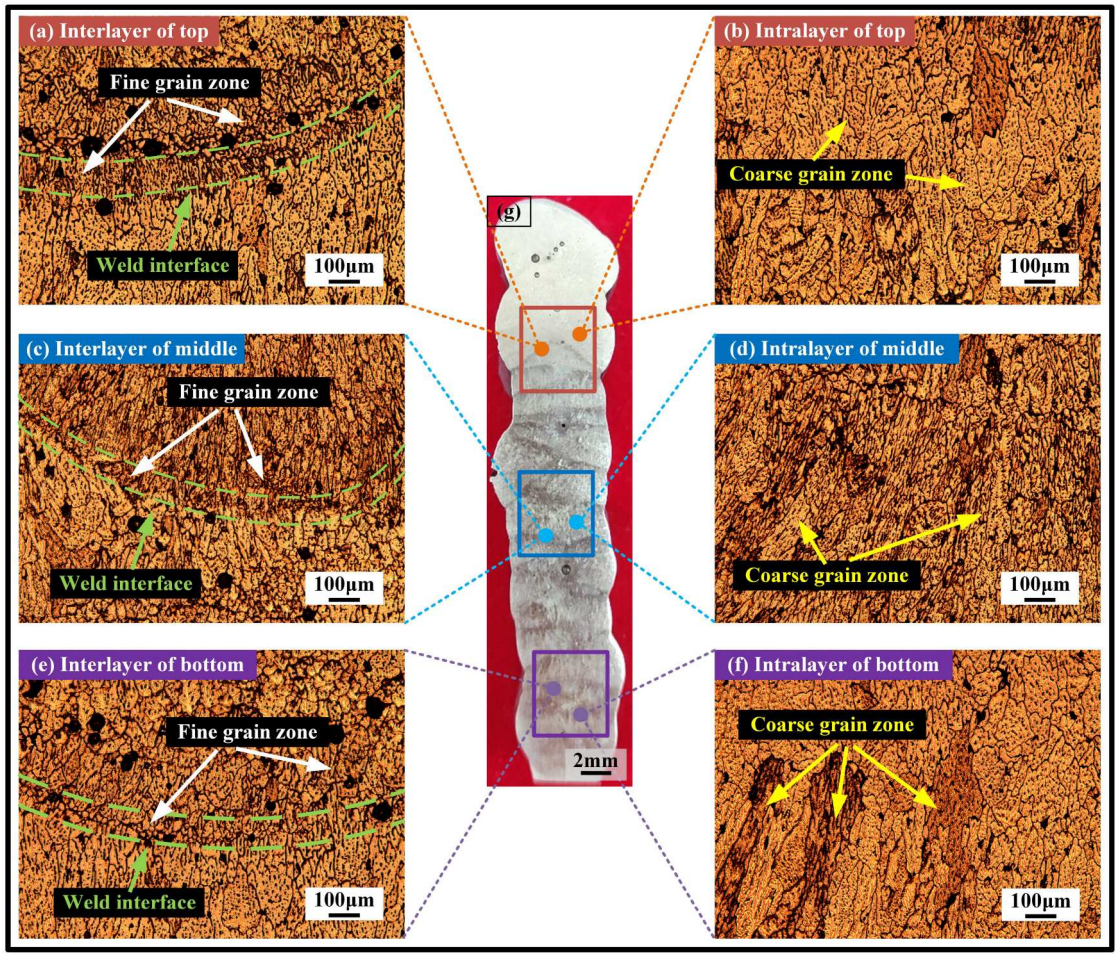

Figure 3. Microstructure of the Al–5.51Cu–0.48Li alloy fabricated component: (a,c,e) interlayer region at the top, middle and bottom of the component, (b,d,f) intralayer region at the top, middle and bottom of the component, (g) longitudinal section of the fabricated component.

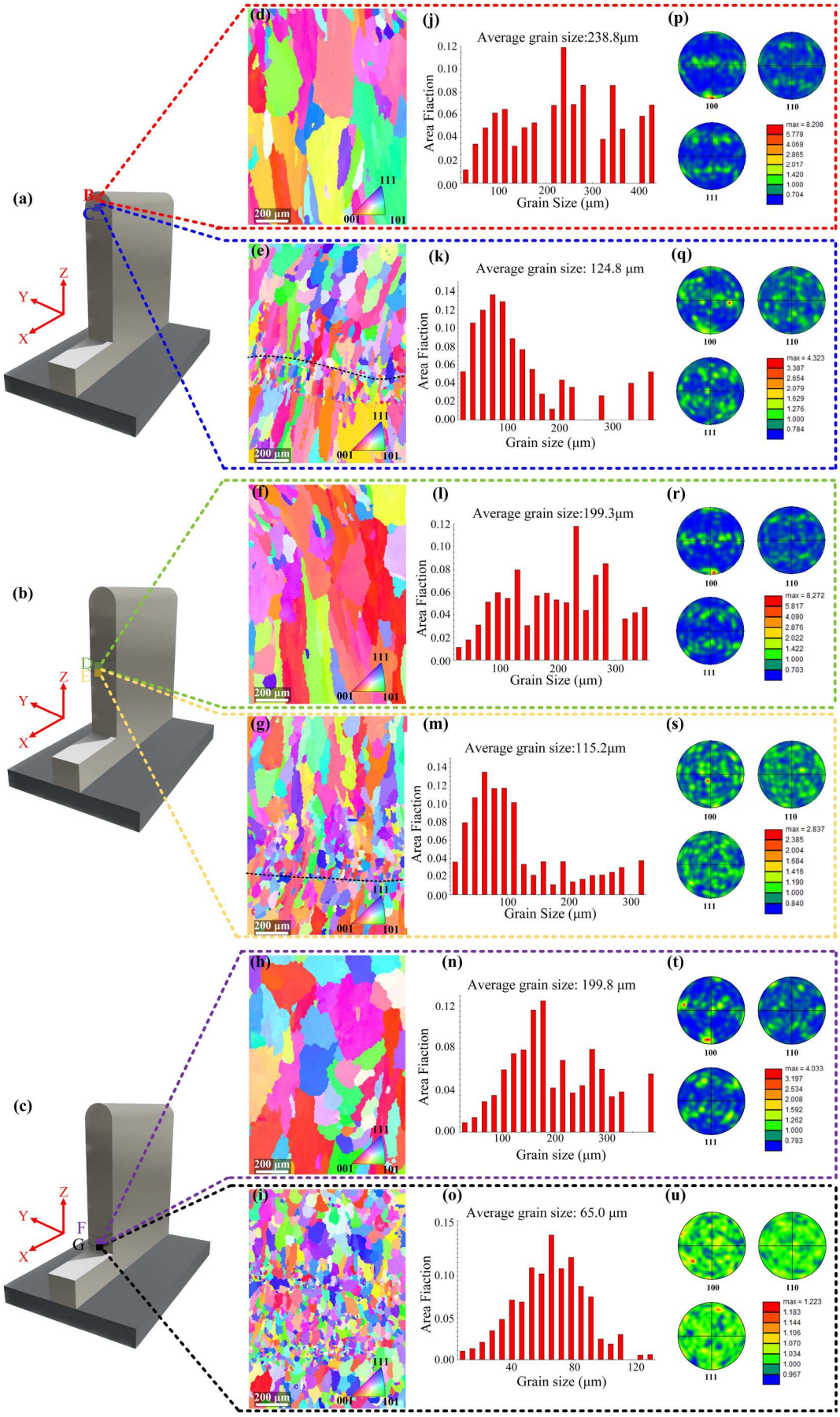

Figure 4. EBSD maps and pole figures analysis of top, middle and bottom layers of the YZ cross-section sample: (a)–(c) scanning positions, (d)–(i) reconstructed grain boundaries, (j)–(o) grain size measurements, (p)–(u) pole figures of regions.

thermal gradients, grains in the [100] direction are often dominant due to their lower surface energies and high growth rates. In AM, the orientation of the grains often coincides with the direction of deposition or heat flow. Due to the motion path of the deposited heat source (arc) and the influence of cooling conditions, the grains tend to grow in a oriented direction. As a result, the texture strength in the [100] direction is usually higher during bypass-GMA DED.

According to the Johnson-Mehl [23] equation, the number of nuclei formed in a given unit time, t, depends on the rate of nucleation, N, and the rate of growth, v_g, as:

$$P(t) = k(\frac{N}{v_g})^{(\frac{3}{4})} \quad (1)$$

where k is a constant, determined by the shape of the crystal nucleus. The nucleation rate and growth rate are determined by the degree of liquid supercooling, ΔT, at the front end of the solid–liquid interface during solidification. The study of Hu et al. [24] shows that $N \propto \exp(\frac{-1}{\Delta T^2})$, and $v_g \propto \Delta T$ where the nucleation rate increases rapidly with the increase of the degree of supercooling. Therefore, due to the high deposition efficiency of the process, the thickness and width of a single layer are thicker (2.2 and 6 mm, respectively), so the degree of supercooling during solidification increases, resulting in a decrease in the number of nucleation events. The larger thickness and width provide sufficient holding time for grain growth to occur. Several independent dendritic grains grow simultaneously in the melt pool, so its orientation becomes more complex, resulting in a larger texture index in the intralayer region and a smaller texture index in the interlayer region. The ratio of nucleation rate, $P(t)$, to nucleation growth rate, v_g, is also small, so coarse grains are obtained in the intralayer region.

By comparing the differences in grain boundary angles between the top, middle and bottom of bypass-GMA DED Al–5.51Cu–0.48Li alloy, it is not only possible to study the differences in their crystal growth behaviours, orientation relations of the grains, and the internal stress states of the grains at the microscopic level, but also provide a reference to the next step of evaluating the differences in their mechanical properties and fracture behaviours.

Figures 5 and 6 detail the grain boundary angles statistics and distribution of bypass-GMA DED Al–5.51Cu–0.48Li alloy, respectively. Generally, grain boundary angles between 2 ∼ 15° are defined as the low-angle grain boundaries (LAGBs) (green curve), and above 15° as high-angle grain boundaries (HAGBs) (blue curve). The HAGBs have a strong hindrance effect, impeding the movement of dislocations and promoting material strengthening. LAGBs have a relatively simple structure and low energy, and they play a 'slip' role in the deformation process within the grain, and their contribution to the change of crystal mechanical properties is relatively small [25,26]. As can be seen from Figure 5, the proportion of HAGBs at different locations is higher than that of LAGBs. Due to the rapid cooling of the deposited layer during additive manufacturing, a large orientation difference between the grains is formed, resulting in a higher proportion of HAGBs. As can be seen from the grain boundary angle distribution in Figure 6, the grain boundary angle distribution near the fusion line is more concentrated due to the recrystallisation of the grains near the fusion line during deposition. Locations with more HAGBs tend to have smaller grains because they inhibit further grain growth. The bottom weave has more HAGBs than the top and middle regions, which promotes recrystallisation, so the grains near the bottom fusion line are small and randomly oriented, as shown in Figures 4(i) and 6(f). In addition, because of heat flow and cooling rates during deposition, grains typically grow in a specific direction, and this directional growth results in greater anisotropy in grain orientation, as shown in Figure 4(d,f). The increase of HAGBs can alleviate the strong bias of this orientation to some extent, as HAGBs can promote the random orientation of the grains, as shown in Figure 4(h).

Figure 7 depicts the Kernel average misorientation (KAM) diagram of bypass-GMA DED Al–5.51Cu–0.48Li alloy. The red-green colour in the figure shows the areas with high KAM values (2 to 5 degrees), which represent the areas of stress concentration. The blue colour indicates areas with low KAM values (0 to 2 degrees) and represents areas with low-density defects. The KAM value inside the deposited alloy grains varies with the morphology and orientation of the grains. The KAM value is higher in the region near the LAGBs, as shown in Figure 7(f). However, the KAM values are lower in the region away from the LAGBs, as shown in Figure 7(d,e). The higher the KAM value, the greater the plastic deformation or stress concentration that the material has undergone. The LAGBs correspond to higher KAM values, which means that the deformation in this region is more uniform and less hindered by dislocations.

3.2. Effect of heat treatment on microstructure of AM components

During deposition, the solidification of the microstructure inside the grain takes precedence over the microstructure at the grain boundary, resulting in the segregation of the Cu element and the eutectic phase

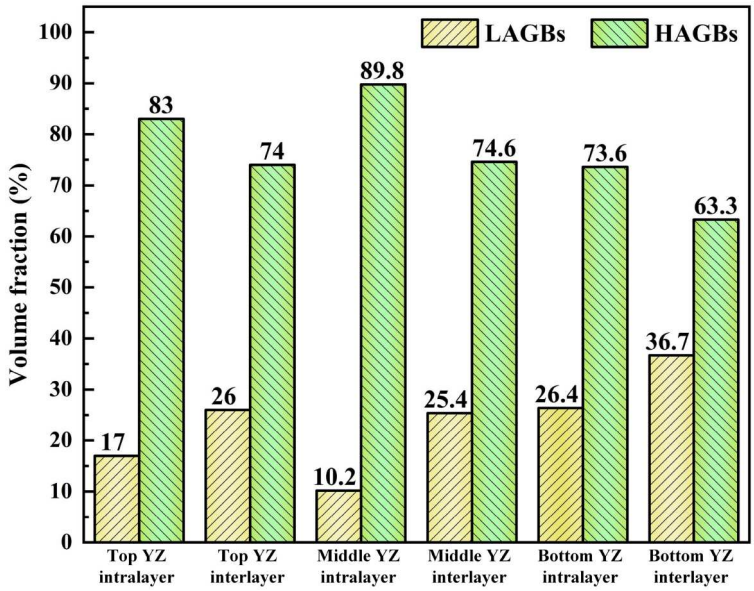

Figure 5. Grain boundary fraction plots of deposited Al–5.51Cu–0.48Li alloy.

with low melting point at the grain boundary, which in turn leads to the 'thickening' of the grain boundary of the deposited alloy, as shown in Figure 8(a,c). The second phase of the deposited alloy is mainly segregated at the grain boundary, with a small amount distributed inside the grain, as shown in Figure 8(c). The segregation of Cu and Al_2Cu phases was eliminated by heat treatment, and Cu was uniformly distributed inside the grain, the eutectic phase with low melting point (α(Al)+θ(Al_2Cu)) at the grain boundary was predominantly dissolved, and a small amount of the high melting point second phase θ(Al_2Cu) was distributed inside the grains, as shown in Figure 8(d). Due to the elimination of segregation, the grain boundaries of the alloy become clearer after heat treatment, as shown in Figure 8(b).

As shown in Figure 9, Al and Al_2Cu phases exist in the deposited 2319 Al alloy (black curve), and after heat treatment, the Al_2Cu phase fraction increases significantly (red curve). In contrast, in the Al–5.51Cu–0.48Li alloy (blue and green curves), in addition to the Al_2Cu phase, two new second phases, Al_2CuLi and δ' (Al_3Li), also formed. After heat treatment, the Al_2Cu phase in Al–5.51Cu–0.48Li alloy decreases, mainly due to the transformation of large particles θ phase into small θ′ and θ″ phases. Meanwhile, Cu aids in the formation of Al_2CuLi, while Al and Li promote Al_3Li formation, resulting in the decrease of peak strength of Al_2Cu phase. In addition, during heat treatment, more Al_2CuLi and Al_3Li phases are formed in the Al–5.51Cu–0.48Li alloys, which significantly increases the diffracted intensity associated to these phases.

The chemical composition of the second phase was studied using HAADF-STEM. As shown in Figure 10, the second phase θ of the deposited 2319 alloy is mainly large particle disc-shaped (Figure 10(a)), while on the deposited Al–5.51Cu–0.48Li alloy is mainly distributed in the shape of short rods (Figure 10(c)). After T6 heat treatment, some large particle dispersion phase remains in 2319 alloy, and a large number of fine needle-like phases appear (Figure 10(b)). Moreover, a large number of fine needle-like phases and a small amount of small dot-like phases appear in Al–5.51Cu–0.48Li alloy after T6 heat treatment (Figure 10(d)). EDS results show that the segregation of Cu and Mn existed inside the deposited 2319 alloy, and the concentration of Cu and Mn in the aluminium matrix is relatively low (Figure 10(a)). The deposited Al–5.51Cu–0.48Li alloy has mainly Cu segregation, and a small amount of Mg, Zn and Zr exist in the aluminium matrix. The increase of these three elements is due to the addition of intermediate alloy components (Figure 10(c)). After the T6 heat treatment, the concentration of Cu inside 2319 alloy matrix significantly increases, and a large number of fine needle-like phases precipitate (θ' and θ''). As the strengthening phases, the size of θ′ phase is about 100–200 nm, while θ'' phase is smaller, about 15–50 nm, with both promoting an increase in the mechanical properties of the alloy (Figure 10(b)). In addition, after the T6 heat treatment, there is still a disc-shaped dispersion phase (θ) in the 2319 alloy. The dispersion phase does not dissolve during the heat treatment, which has no effect on the mechanical properties of the material, but can provide nucleation sites for the

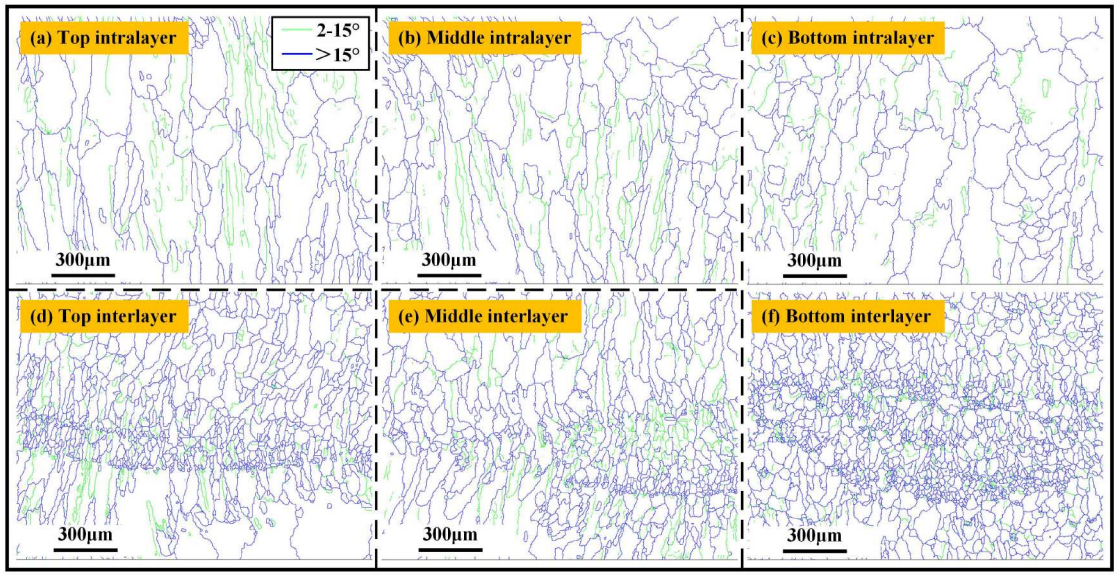

Figure 6. Grain boundary distribution of deposited Al–5.51Cu–0.48Li alloy: (a) top intralayer, (b) middle intralayer, (c) bottom intralayer, (d) top interlayer, (e) middle interlayer, (f) bottom interlayer.

needle-like phase to form and accelerate its precipitation (Figure 10(b)). After T6 heat treatment, the Cu-containing phase θ in the Al–5.51Cu–0.48Li alloy is almost completely dissolved, and the concentration of Cu increases significantly, which is significantly higher than the increase of Cu concentration in T6 2319 alloy. Such a high concentration of Cu provides the precursor Guinier-Preston (GP) zones (Cu enrichment) for the strengthening phase, so the precipitation content and rate of the strengthened phase are increased (Figure 10(d)).

Compared to two kinds of strengthening phases (θ′ and θ″) precipitated from T6 2319 alloy, four kinds of strengthening phases are precipitated inside the T6 Al–5.51Cu–0.48Li alloy, namely θ', θ'', T_1 and δ' phases (Figure 10(c)). Among them, θ', θ'' and T_1 are needle-like phases, but they are differ in size and content. The length of θ' and T_1 phases is about 100–200 nm, but the width of the θ' phase is higher, its fraction is increased, and their orientation is well defined. In opposition, the T_1 phase is finer, its content is lower, and upon their formation there exists an orientation relationship

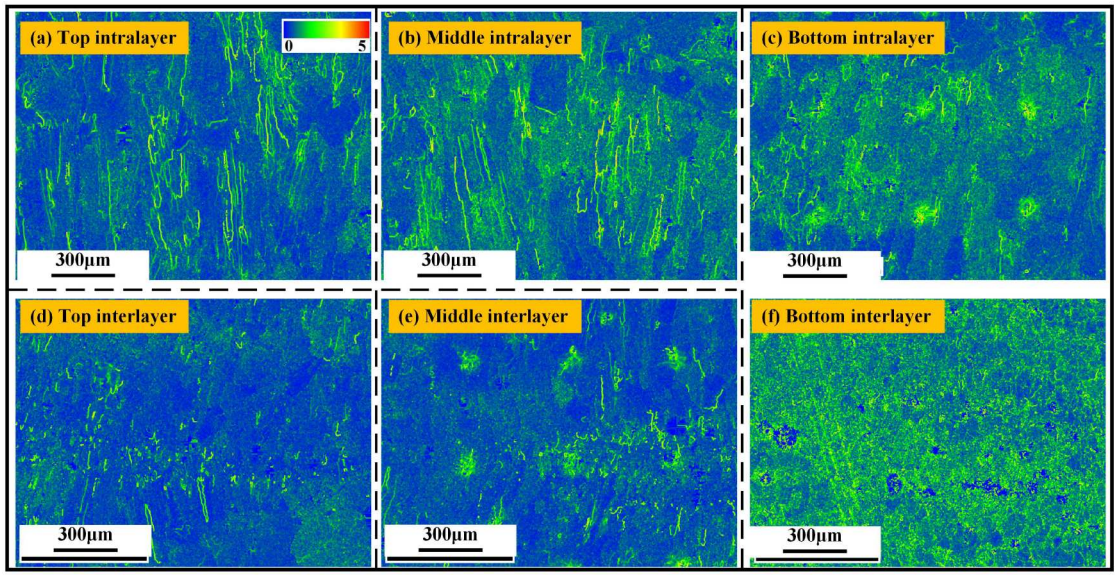

Figure 7. KAM diagram of deposited Al–5.51Cu–0.48Li alloy: (a) top intralayer, (b) middle intralayer, (c) bottom intralayer, (d) top interlayer, (e) middle interlayer, (f) bottom interlayer.

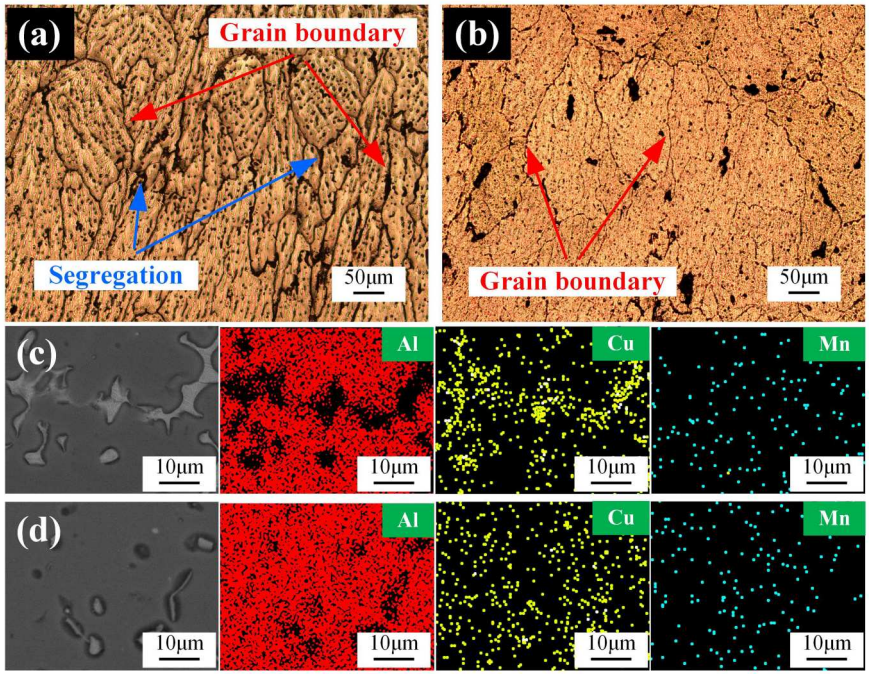

Figure 8. OM and SEM of Al–5.51Cu–0.48Li alloy fabricated component: (a) deposited state, (b) T6 heat treatment state: (a) and (b) are OM before and after heat treatment, and (c) and (d) are SEM before and after heat treatment, respectively.

with the θ' phase. Studies [27] show that, in the direction of [110] Al incidence, the relationship between T_1 phase and θ' phase is 125.3°, and the relationship between T_1 phase and T_1 phase is 109.4°. The rod-like θ″ phase formed is shorter, with its size ranging from about 15 to 50 nm (Figure 10(d)). In addition, the increase of the types and quantities of strengthening phases in Al–5.51Cu–0.48Li alloys lays a foundation for the improvement of mechanical properties.

To more accurately analyse the microstructure of the second phase formed, high-resolution transmission electron microscopy was used to characterise the lattice fringes of the second phase, and all images were obtained from the [110] Al orientation, as shown in Figure 11. The lattice fringe spacing of Al matrix, θ phase, θ′ phase, θ″ phase, δ′ phase and T_1 phase in Al–5.51Cu–0.48Li alloy is 0.2152, 0.1299, 0.2907, 0.2127, 0.2205 and 0.2550 nm, respectively. It can be seen that θ phase is completely irrelevant to Al matrix, and has little effect on the properties of Al matrix (Figure 11(d)). From the electron diffraction pattern of [110] Al crystal band axis, it can be seen that the diffraction spots of δ' phase and T_1 phase are at the red circles in Figure 11(d,e), respectively. Thus, the relationship between δ' phase and T_1 phase and Al matrix is completely coherent and semi-coherent, respectively. In addition, the lattice fringe spacing of θ″ phase is close to Al matrix, and the relationship with Al matrix is completely coherent (Figure 11(c)). The lattice fringe spacing of θ' phase is quite different from that of Al matrix, and is semi-coherent with Al matrix (Figure 11(b,e)). Therefore, δ′, θ′, θ″ and T_1 phases can optimise the microstructure and properties of the alloy, in which δ′ and θ″ which are completely coherent with the Al matrix have the greatest influence on the microstructure and properties of the alloy.

3.3. Effect of heat treatment on mechanical properties of AM components

Figure 12 shows the comparison of tensile properties of GMA DED 2319 alloy and bypass-GMA DED Al–5.51Cu–0.48Li alloy. Figure 12(a) shows the longitudinal tensile stress–strain curves of 2319 alloy and Al–5.51Cu–0.48Li alloy before and after T6 heat treatment. The tensile strength and elongation of the 2319 alloy in the deposited state are 254 MPa and 13.1% (blue curve), and the strength and elongation of 2319 alloy after T6 heat treatment are 372 MPa and 5.9% (black curve), respectively. The tensile strength and elongation of the deposited Al–5.51Cu–0.48Li alloy are 310 MPa and 3.0% (red curve), respectively, and 492 MPa and 2.5% (green curve) after T6 heat treatment. Compared to the deposited and T6 2319 alloy, the tensile strength of the deposited and T6 Al–5.51Cu–0.48Li alloys is increased by 21.9% and 32.3%, respectively. Figure 12(b) depicts the longitudinal and transverse stress–strain curves of Al–5.51Cu–0.48Li alloy before and

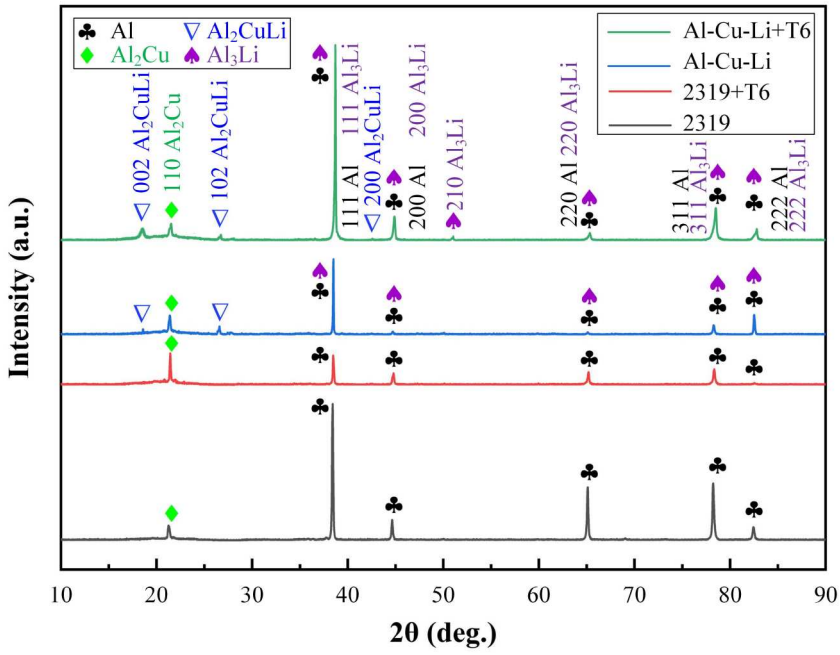

Figure 9. XRD patterns of 2319 Al alloy and Al–5.51Cu–0.48Li alloy before and after heat treatment.

after heat treatment, and Figure 12(d) details the longitudinal and transverse tensile strength, yield strength and elongation of Al–5.51Cu–0.48Li alloy before and after heat treatment. Compared to the longitudinally deformed samples (black and blue curves), the elongation and tensile strength of the transverse counterparts have significantly improved mechanical response (red and green curves). Figure 12(c) shows the longitudinal and transverse tensile strength and elongation of GMA DED 2319 alloy. The longitudinal and transverse tensile strength of GMA DED 2319 alloy in deposition state are 254 and 257 MPa respectively. After T6 heat treatment, the tensile strength of 2319 alloy is increased to 372 and 383 MPa respectively. The longitudinal tensile strength, yield strength and elongation of the deposited Al–5.51Cu–0.48Li alloy are 310, 227 MPa and 3.0% (Figure 12(d)), respectively. After T6 heat treatment, the longitudinal tensile strength, yield strength and elongation are 492, 440 MPa and 2.5% (Figure 12(d)), respectively. The transverse tensile strength, yield strength and elongation of the deposited Al–5.51Cu–0.48Li alloy are 371, 250 MPa and 5.18% (Figure 12(d)), respectively, and the transverse tensile strength, yield strength and elongation of the deposited Al–5.51Cu–0.48Li alloy after T6 heat treatment are 591, 416 MPa and 5.15% (Figure 12(d)), respectively. Compared to the deposited alloy, the longitudinal tensile strength and yield strength of T6 heat treatment increased by 58.6% and 93.2%, respectively, and the elongation decreased by 16.7%. After T6 heat treatment, the transverse tensile strength and yield strength are increased by 59.2% and 66.1%, respectively, and the elongation is decreased by 0.6%.

In summary, the mechanical properties of the two deposited alloys are different, mainly because the addition of Li element optimises the distribution and morphology of the second phase. The addition of Li element can promote the uniform distribution of the second phase, reduce the precipitation of large particles from the second phase, and form a finer, uniformly dispersed particle or rod-like structure. This refined second phase helps to stop the slippage of the dislocation, thereby enhancing the strength of the material. The strength of the alloy after heat treatment is greatly increased because a large number of fine needle-like strengthening phases are precipitated after aging. These needle-like second phases form a coherent and semi-coherent interface with the Al matrix, which can be well embedded in the matrix lattice and reduce the interface energy, and can effectively contain the dislocation, increase the difficulty of dislocation traversal, and thus enhance the strength of the alloy. The strength of Al–5.51Cu–0.48Li alloy after T6 heat treatment is higher than that of 2319 Al alloy, because the addition of Li element promotes the precipitation of more types of needle-like strengthening phases in Al–5.51Cu–0.48Li alloy. The 2319 Al alloy only precipitates θ′ and θ″ two strengthened phases, while Al–5.51Cu–0.48Li precipitates θ′, θ″, δ′ and T_1 phases.

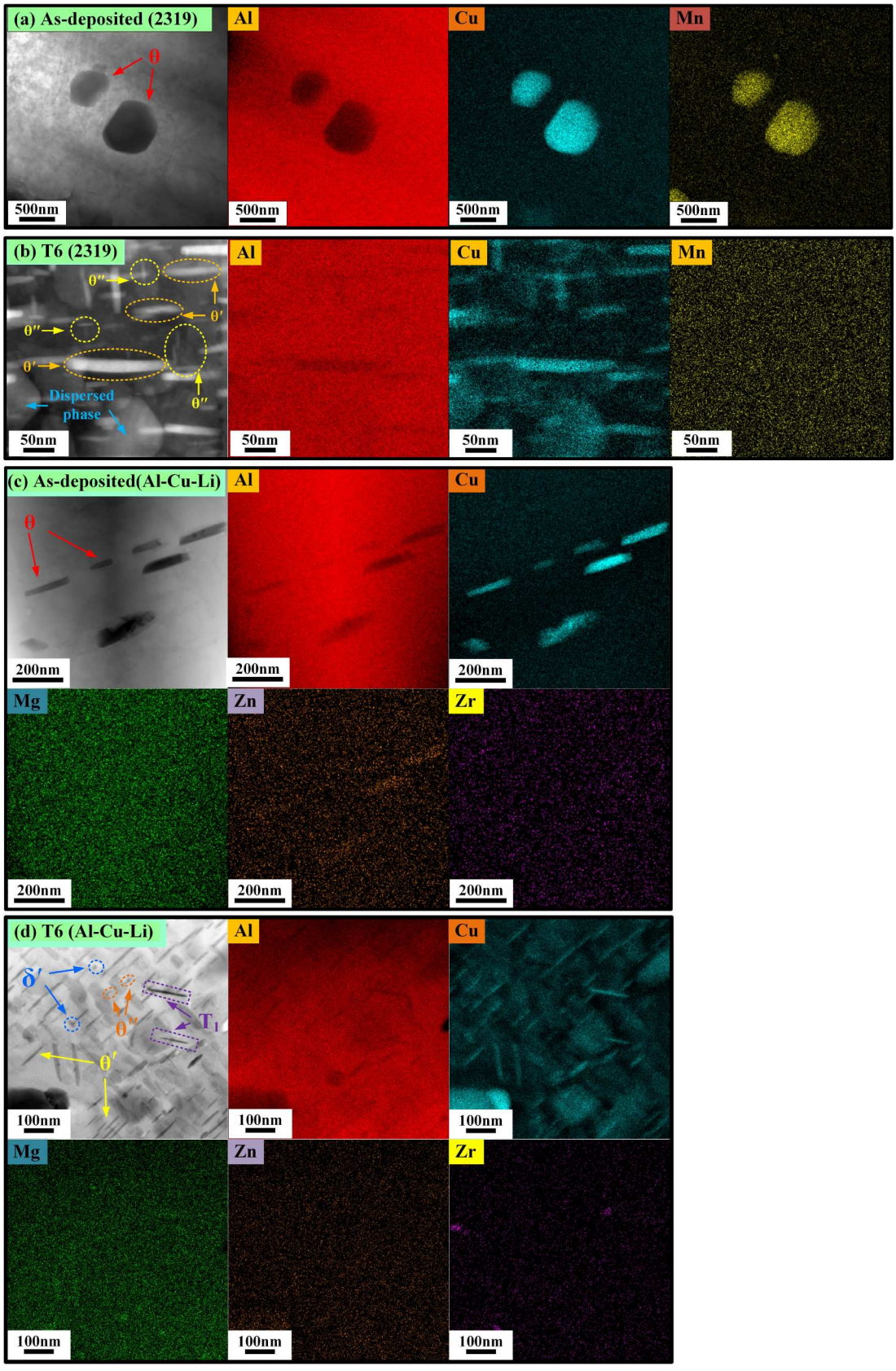

Figure 10. HAADF-STEM image and EDS mapping of second phase: (a) deposited 2319 alloy; (b) T6 heat treatment of 2319 alloy (c) deposited Al–5.51Cu–0.48Li alloy; (d) T6 heat treatment of Al–5.51Cu–0.48Li alloy.

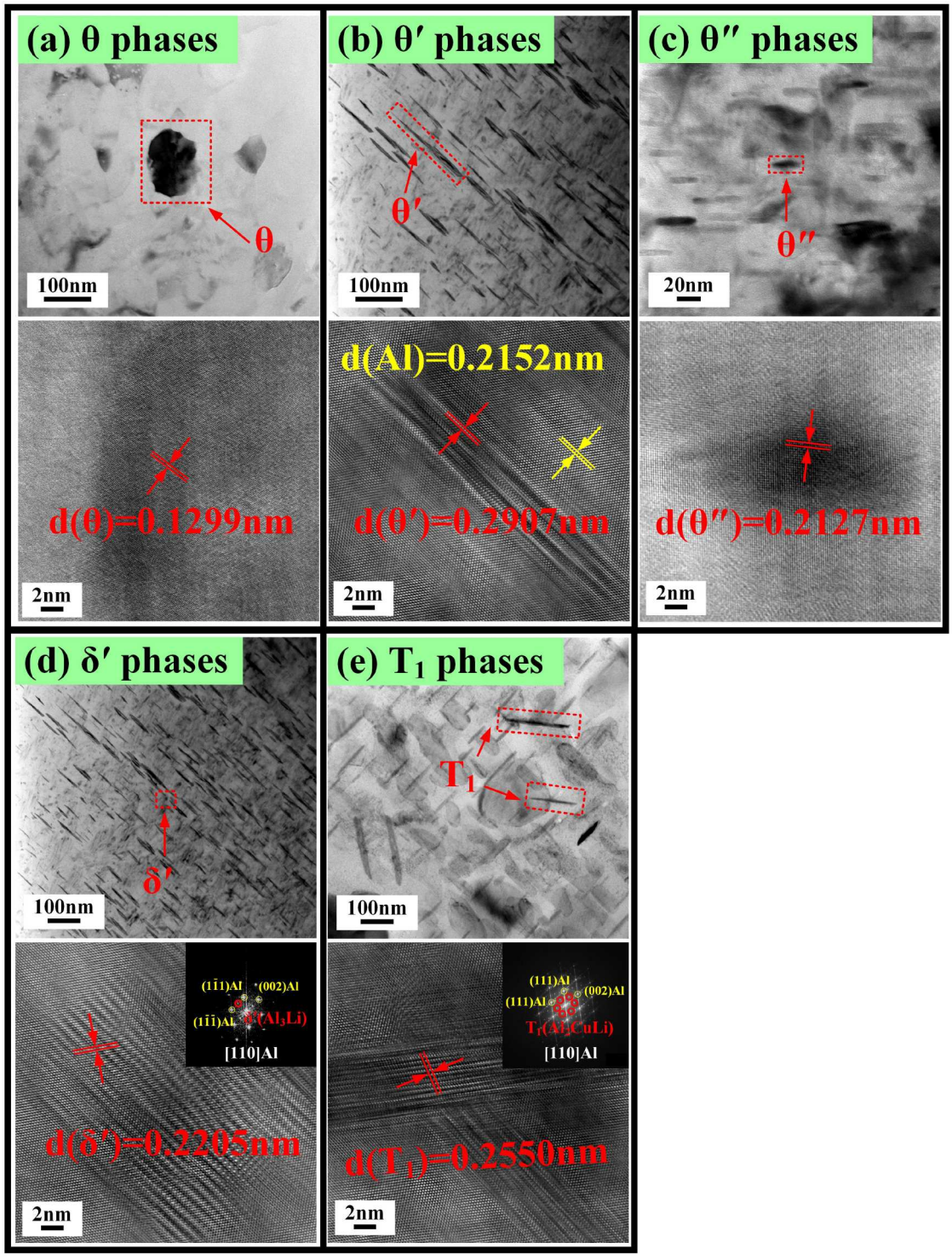

Figure 11. Magnified HRTEM image for second phase analysis in Al–5.51Cu–0.48Li alloy fabricated by bypass-GMA DED: (a) θ phase; (b) θ' phase; (c) θ'' phase; (d) δ' phase; (e) T_1 phase.

According to Liu et al. [28], the predicted strength, σ, of an Al–5.51Cu–0.48Li alloy prepared by bypass-GMA DED must include grain boundary strengthening, solid solution strengthening and precipitation strengthening:

$$\sigma = \sigma_0 + \Delta\sigma_{gb} + \Delta\sigma_{ss} + \Delta\sigma_{or} \quad (2)$$

where σ_0 is the tensile strength of pure Al (80 MPa), $\Delta\sigma_{gb}$, $\Delta\sigma_{ss}$ and $\Delta\sigma_{or}$ are the strength increment caused by grain boundary, solid solution and precipitation effects, respectively.

The average grain size in the central region is about 182 μm. According to the Hall-Petch

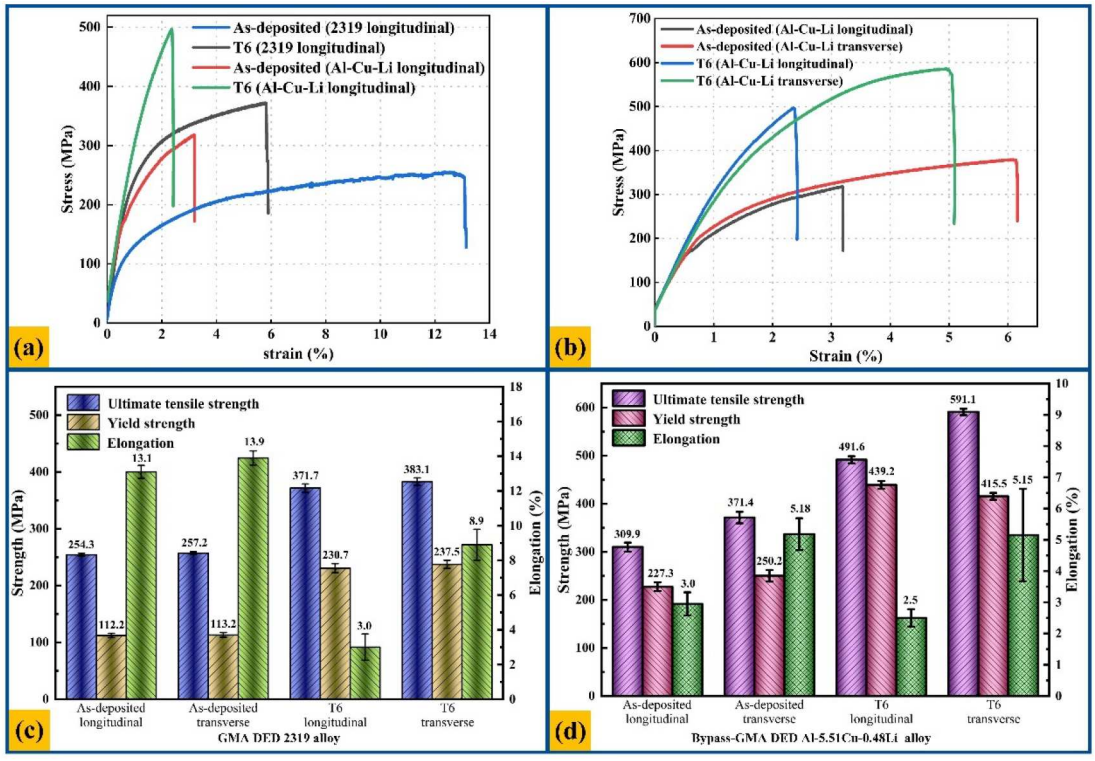

Figure 12. Comparison of mechanical properties of AMed 2319 alloy and Al–5.51Cu–0.48Li alloy before and after heat treatment: (a) longitudinal tensile stress–strain curves of 2319 alloy and Al–5.51Cu–0.48Li alloy before and after heat treatment; (b) longitudinal and transverse tensile stress–strain curves of Al–5.51Cu–0.48Li alloy before and after heat treatment; (c) tensile properties of 2319 alloy before and after heat treatment; (d) tensile properties of Al–5.51Cu–0.48Li alloy before and after heat treatment.

relationship, grain boundary strengthening is defined as [29]:

$$\Delta\sigma_{gb} = k_y d^{\frac{-1}{2}} \tag{3}$$

where k_y is the Hall-Petch coefficient (0.14 MPa·mm$^{1/2}$), the calculated $\Delta\sigma_{gb}$ is 10 MPa, and the contribution of solid solution strengthening is as follows [30]:

$$\Delta\sigma_{ss} = \sum_i k_i C_i \tag{4}$$

where k_i is the strength increase efficiency of each element (k_{Zn} = 2.9 MPa/wt.%, k_{Mg} = 18.6 MPa/wt.%, k_{Cu} = 13.8 MPa/wt.%, k_{Li} = 10.9 MPa/wt.% [31]). C_i represents the solute content, Cu, Li, Mg, Zn and Mn contents are 5.51%, 0.48%, 0.18%, 0.26% and 0.29% respectively, and the calculated value of $\Delta\sigma_{ss}$ is 89 MPa. Orowan mechanism is the main mechanism of θ', θ'', δ' and T_1 strengthening in Al–Cu–Li alloys [31]. The contribution of Orowan mechanism enhancement is expressed by [28,32]:

$$\Delta\sigma_{or} = M\frac{0.4Gb}{\pi\sqrt{1-v}}\frac{\ln(2r/b)}{\lambda} \tag{5}$$

$$\lambda = \sqrt{\frac{3\pi}{4f}} - 1 \tag{6}$$

where M is the Taylor factor (3.06 for FCC alloy), G is the shear modulus (26.5 GPa for Al matrix), v is Poisson's ratio (0.34), and b is the Burgers vector (0.286 nm for Al alloy). r (estimated at 7 nm based on HRTEM images) and f (estimated at 12.8% based on SEM and HRTEM images) are the mean radii and volume fractions of θ', θ'', δ' and T_1 precipitates. The calculated $\Delta\sigma_{or}$ is 430 MPa. The predicted strength σ of Al–5.51Cu–0.48Li alloy is 609 MPa (σ_0 = 80 MPa, $\Delta\sigma_{gb}$ = 10 MPa, $\Delta\sigma_{ss}$ = 89 MPa, $\Delta\sigma_{or}$ = 430 MPa). The transverse tensile strength of the component is 591 MPa, which almost reaches the predicted value. Compared to the transverse samples, the longitudinal tensile fracture occurs at the interlayer fusion line, which is region that accumulates pores, resulting in a lower tensile strength in longitudinally deformed material.

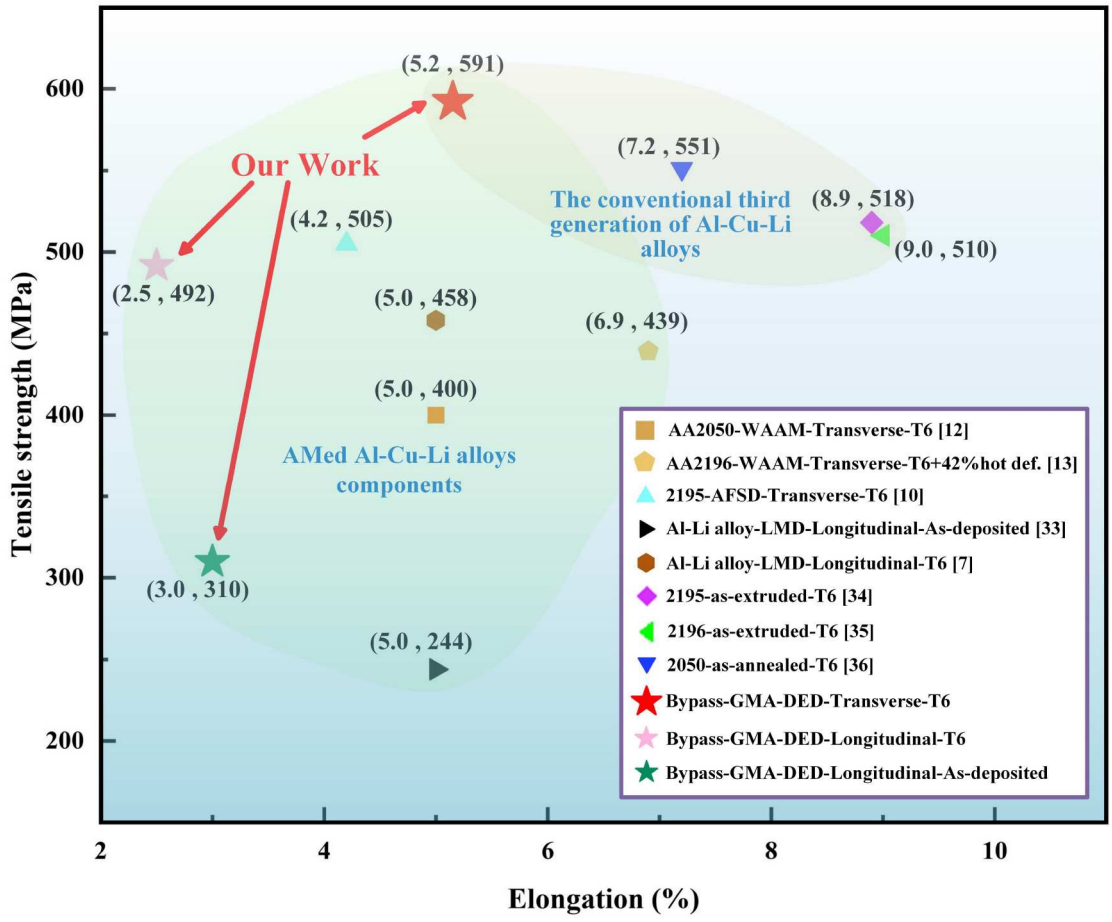

Figure 13. Comparison of tensile strength and elongation of Al–Cu–Li alloys with different processes.

Figure 13 shows the relationship of the mechanical properties of Al–Cu–Li alloys under different processes. As shown in Figure 13, the three different colour asterisks represent the transverse properties of T6 state Al–5.51Cu–0.48Li alloy (red asterisk), the longitudinal properties of T6 state Al–5.51Cu–0.48Li alloy (pink asterisk), and the longitudinal properties of deposited state Al–5.51Cu–0.48Li alloy (dark green asterisk), respectively. Compared to the current Al–Cu–Li alloy components by different AM methods, the longitudinal tensile strength of the as-deposited state (310 MPa) and T6 state (492 MPa) in this study is higher than that of the LMD as-deposited state (244 MPa) [33] and T6 state (458 MPa) [7], respectively. The transverse tensile strength of the T6 state Al–5.51Cu–0.48Li alloy (591 MPa) is also higher than that of the WAAM AA2050-T6 (400 MPa) [12], WAAM AA2196-T6 + 42% hot deformation (439 MPa) [13] and AFSD 2195-T6 (505 MPa) [10], respectively. Compared to the conventional third generation Al–Cu–Li alloys prepared by traditional processes, the transverse tensile strength 591 MPa (T6 state) is still higher than that of the 518 MPa (as-extruded 2195-T6) [34], 510 MPa (as-cast 2196-T6) [35] and 551 MPa (as-annealed 2050-T6) [36], respectively. Although there are a small number of pores in the Al–5.51Cu–0.48Li alloy deposited in this study, as shown in the metallographic diagram in Figure 3. Nonetheless, through reasonable AM process parameter optimisation, heat treatment process development and composition design, the transverse tensile strength of the alloy reached 591.1 MPa, which was higher than that of AMed Al–Cu–Li alloys and met the performance requirements of the third generation Al–Cu–Li alloy.

In order to compare the mechanical property differences between different materials, several mechanical property parameters need to be considered in engineering design. A parameter Q can be used as a basis for the comprehensive consideration of these parameters, providing more comprehensive information and guidance for material selection, design and application, which makes the materials perform better in practical applications.

However, the elongation of the bypass-GMA DED Al–5.51Cu–0.48Li alloy is relatively low. In order to quantify comprehensively the properties of the formed alloy, a parameter Q is introduced. Q as defined by the

Table 4. *Q* values of T6 Al–Cu–Li alloy under different preparation processes.

Grade and state	Tensile strength (MPa)	Elongation (% El)	*Q* (MPa)
Our work-T6	591	5.2	715
2050-as-annealed-T6 [36]	551	7.2	680
AA2196-WAAM-T6 + 42% hot [13]	439	6.9	565
2195-AFSD-T6 [10]	505	4.2	598
Al–Li alloy-LMD-as-deposited [33]	244	5.0	349
Al–Li alloy-LMD-T6 [7]	458	5.0	563
2195-as-extruded-T6 [34]	518	8.9	660
2196-as-extruded-T6 [35]	510	9.0	653
AA2050-WAAM-T6 [12]	400	5.0	505

UTS(*MPa*) and elongation (%*El*):

$$Q = UTS(MPa) + 150 \times \log(\%El) \tag{7}$$

As is shown in Table 4, the value *Q* (715 MPa) of T6 state Al–5.51Cu–0.48Li alloy prepared by bypass-GMA DED method is higher than that of T6 state LMD Al–Li alloy (563 MPa) [7], T6 state WAAM AA2050 (505 MPa) [12], T6 state WAAM AA2196 (565 MPa) [13], T6 state AFSD 2195 (598 MPa) [10], T6 state as-extruded 2195 (660 MPa) [34], T6 state as-extruded 2196 (653 MPa) [35] alloys and T6 state as-annealed 2050 alloy (680 MPa) [36]. The results show that the Al–5.51Cu–0.48Li alloy prepared by bypass-GMA DED method has better mechanical properties. This novel bypass-GMA DED has the advantages of large single-layer size and low subcooling degree ΔT, attributed to the larger grain size unfortunately. In the future, the heterogeneous nucleation during melt pool solidification can be increased by adding grain refiners [37], so as to achieve grain refinement and further improve the mechanical properties of the prepared alloys.

Figure 14 shows the micro-hardness comparison between 2319 alloy and Al–5.51Cu–0.48Li alloy before and after heat treatment. The deposited 2319 alloy has low micro-hardness and relatively small fluctuation of micro-hardness value (purple curve), while the deposited Al–5.51Cu–0.48Li alloy has a slight increase in micro-hardness value but relatively large fluctuation of micro-hardness value (green curve). After T6 heat treatment, the micro-hardness of 2319 alloy and Al–5.51Cu–0.48Li alloy increased significantly, and the micro-hardness values of both fluctuated relatively large (brown curve and red curve), as shown in Figure 14(a). The average micro-hardness of deposited 2319 alloy and Al–5.51Cu–0.48Li alloy is 70.2 and 92.4 HV (purple column and green column), and the average micro-hardness of T6 state 2319 alloy and Al–5.51Cu–0.48Li alloy is 131.1 and 146.4 HV, respectively. Compared with the deposited and T6 state 2319 alloy, the average micro-hardness of Al–5.51Cu–0.48Li alloy increases by 31.6% and 11.7% respectively, as shown in Figure 14(b).

In summary, the hardness of the 2319 Al and 5.51Cu–0.48Li Al–Li alloys changes periodically along the deposition direction, which is mainly related to grain structure, porosity and phase transformation characteristics. In areas of higher peak temperature or slower cooling, grains will grow larger, and larger grains provide fewer grain boundaries, so the material has less resistance to deformation, resulting in a decrease in material hardness. The smaller the grain structure, the stronger the resistance to deformation of the material, and therefore the hardness. The presence of porosity can lead to a local reduction in the hardness of the material, as these defects act as stress concentration points that can cause local plastic deformation upon loading. In addition, during the hot

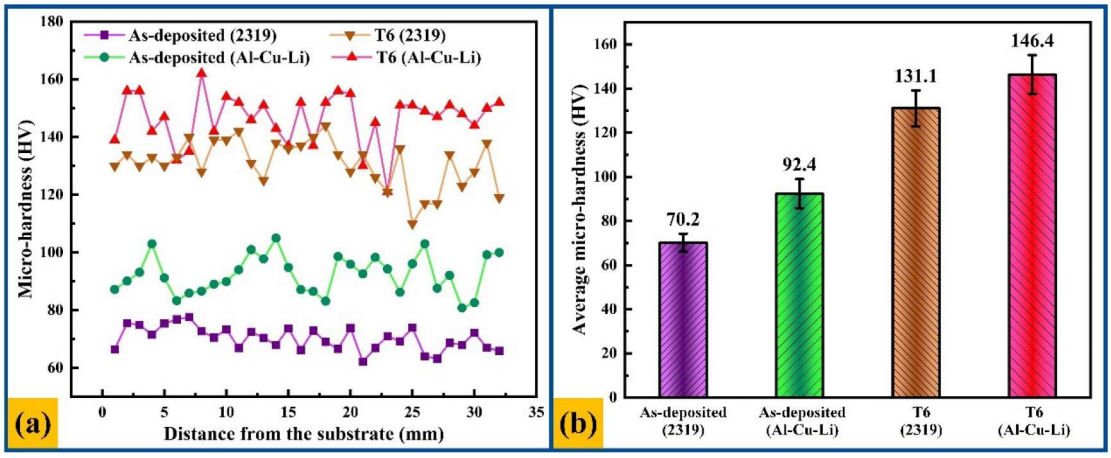

Figure 14. Comparison of micro-hardness of 2319 alloy and Al–5.51Cu–0.48Li alloy before and after heat treatment in YZ section: (a) micro-hardness point plot; (b) average micro-hardness.

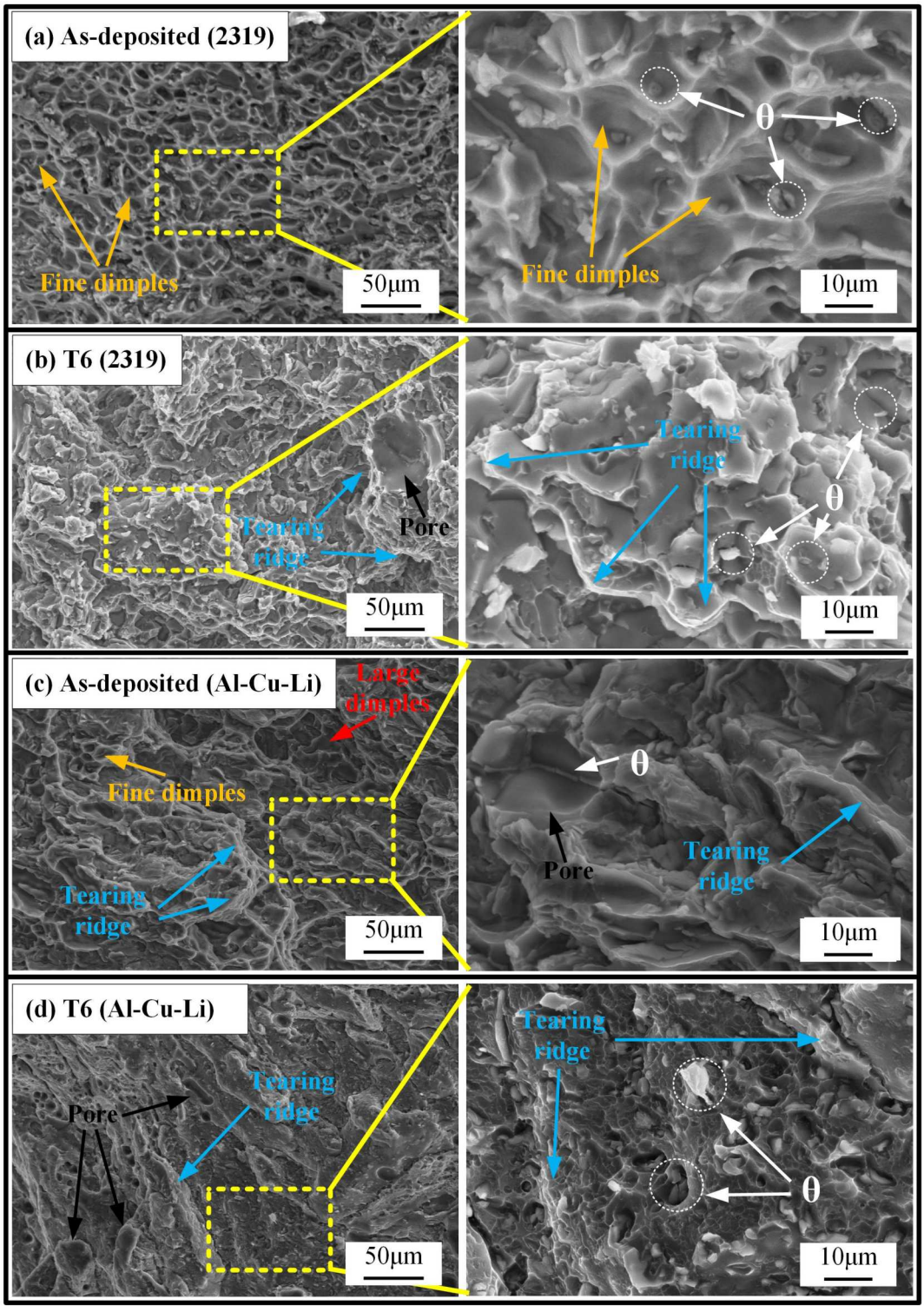

Figure 15. Longitudinal fracture analysis of 2319 alloy and Al–5.51Cu–0.48Li alloy before and after heat treatment: (a) deposited 2319 alloy; (b) T6 state 2319 alloy; (c) deposited Al–5.51Cu–0.48Li alloy; (c) T6 state Al–5.51Cu–0.48Li alloy.

deposition process, the phase transformation behaviour of alloys (such as the formation of solid solutions, changes in precipitated phases) will be affected by temperature, which in turn will affect the hardness of deposited material.

Upon the addition of Li element, the solid solution strengthening effect is enhanced, resulting in higher strength and micro-hardness of the deposited Al–5.51Cu–0.48Li alloy, when compared to the 2319 alloy. Due to the rapid diffusion rate of Li during the heat

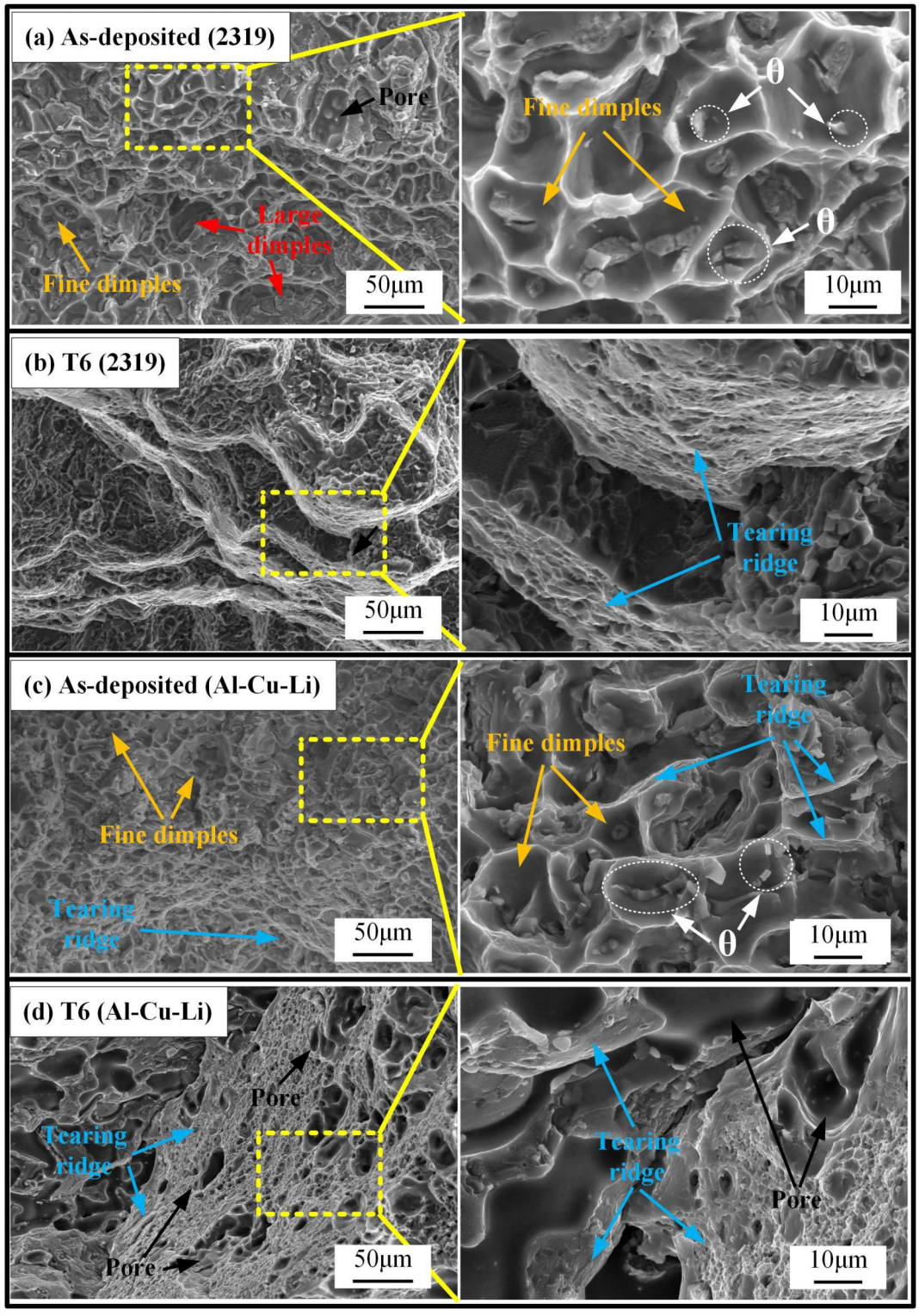

Figure 16. Transverse fracture analysis of 2319 alloy and Al–5.51Cu–0.48Li alloy before and after heat treatment: (a) deposited 2319 alloy; (b)T6 state 2319 alloy; (c) deposited Al–5.51Cu–0.48Li alloy; (c) T6 state Al–5.51Cu–0.48Li alloy.

treatment, the precipitation of δ' phase and T_1 phase in Al–5.51Cu–0.48Li alloy is increased, which further aids in increasing the strength and micro-hardness of Al–5.51Cu–0.48Li alloy after the T6 heat treatment.

To analyse the fracture characteristics of the 2319 and Al–Cu–Li alloys, the longitudinal fracture morphology after deformation was probed by SEM. As shown in Figure 15, a large number of small and shallow

dimples (orange arrows) are mainly distributed in the longitudinal fracture surface of the deposited 2319 alloy, showing a typical ductile fracture. The second phase θ (white arrows) is mainly distributed in the centre of the dimple, while some evidence of this phase can be found distributed along the grain boundaries (Figure 15(a)). In addition to the distribution of small and shallow dimples (orange arrow), there are also some large and deep dimples (red arrow) at the longitudinal fracture surface of the deposited Al–5.51Cu–0.48Li alloy. In addition, there is also evidence of tearing edges of different sizes (blue arrows) at the fracture surface. Therefore, the fracture characteristics are the combination of ductile and brittle aspects, and the second phase θ (white arrows) are distributed at the grain boundaries. As shown in Figure 15(c), after the T6 heat treatment, both the 2319 alloy and Al–5.51Cu–0.48Li alloy show brittle fracture characteristics, with a large number of tearing edges (blue arrows) distributed at the fracture surface. However, the Al–5.51Cu–0.48Li alloy has more tearing edges and these features are larger compared to the 2319 counterpart (Figure 15(b,d)). A large fraction of granular θ phase (white arrows) are distributed at the fracture surface of both materials. These irregular second phases are equivalent to intermetallic compounds and will reduce the toughness of the materials.

A large number of small and shallow dimples (orange arrows) are also distributed in the transverse fracture of both 2319 alloy and Al–5.51Cu–0.48Li alloy, and the second phase θ particles are distributed in the centre of the dimples, among which the second phase θ is larger in the dimples of 2319 alloy (refer to Figure 16(a,c)). In addition, there are some large and deep dimples at the fracture surface of the deposited 2319 alloy (red arrows), and some tearing edges at the fracture of the deposited Al–5.51Cu–0.48Li alloy (blue arrows). Therefore, the deposited 2319 alloy shows evidence of a ductile fracture, while the deposited Al–5.51Cu–0.48Li alloy shows tough-brittle composite fracture, as shown in Figure 16(a,c). After the T6 heat treatment, both 2319 alloy and Al–5.51Cu–0.48Li alloy show brittle fracture, with a large number of tearing edges (blue arrows) distributed at the fracture, with the Al–5.51Cu–0.48Li alloy has longer tearing edges (see Figure 16(b,d)).

4. Conclusion

In this work, a novel bypass-GMA DED-arc method was proposed. An Al–5.51Cu–0.48Li alloy was synthesised in situ by this method, and the alloy was subjected to T6 heat treatment. The evolution and improvement of microstructure and mechanical properties of the alloy before and after heat treatment were studied. The main conclusions are as follows:

(1) The composition of the prepared Al–5.51Cu–0.48Li alloy ((Li) = 0.48wt.%) is close to that of the theoretical calculations ((Li) = 0.50wt. ~ 0.62wt.%). The Cu/Li ratio (11.5) is in line with the development trend of the third generation Al–Cu–Li alloys ((Cu) > 2.5wt.%; (Li) < 2.0wt.%), possessing better mechanical properties with low Li content (0.48 wt.%).
(2) The grain structure of Al–5.51Cu–0.48Li alloy components prepared by bypass-GMA DED has typical periodic characteristics. The interlayer grains are coarse columnar grains, while the interlayer regions are mainly fine equiaxed grains. Accordingly, the average grain size of the intralayer region is higher than that of the interlayer in the top YZ section, middle YZ section and middle XZ section. The grain texture characteristics in the intralayer region are also stronger than the interlayer region.
(3) During the subsequent heat treatment process, only two strengthening phases (θ′ and θ″) appeared in the 2319 alloy. Due to the addition of Li element and the high diffusion rate of Li, four kinds of strengthening phases (θ', θ'', δ' and T_1) appear in Al–5.51Cu–0.48Li alloy after aging, which can increase the mechanical properties of the alloy.
(4) After T6 heat treatment, the average micro-hardness, longitudinal and transverse tensile strength of the prepared Al–5.51Cu–0.48Li alloy components increased, while the longitudinal and transverse elongation decreased. The fracture of the samples changed from a composite fracture of toughness and brittleness to the brittle fracture, and the fracture characteristics changed from a large number of dimples to large tearing edges.
(5) Compared to other AM and casting Al–Cu–Li alloys, the alloy Al–5.51Cu–0.48Li has better mechanical properties. The strength of the fabricated parts reached the level of the conventional third generation Al–Cu–Li alloys.

Disclosure statement

No potential conflict of interest was reported by the author(s).

Funding

This work was supported by National Natural Science Foundation of China [grant number 52475343], Central Guidance for Local Scientific and Technological Development Funding Projects [grant number 246Z1015G] and Natural Science Foundation of Hebei Province [grant number E2024208049]. JPO

acknowledges funding by national funds from FCT – Fundação para a Ciência e a Tecnologia, I.P., in the scope of the projects LA/P/0037/2020, UIDP/50025/2020 and UIDB/50025/2020 of the Associate Laboratory Institute of Nanostructures, Nanomodelling and Nanofabrication – i3N.

Data availability statement

The data supporting the findings of this study are openly available in Mendeley Data at https://doi.org/10.17632/rpdhyzh899.1.

ORCID

J. P. Oliveira http://orcid.org/0000-0001-6906-1870

References

[1] Lewandowski JJ, Seifi M. Metal additive manufacturing: a review of mechanical properties. Annu Rev Mater Res. 2016;46(1):151–186. doi:10.1146/annurev-matsci-070115-032024

[2] Frazier WE. Metal additive manufacturing: a review. J Mater Eng Perform. 2014;23(6):1917–1928. doi:10.1007/s11665-014-0958-z

[3] Zhang X, Xiao Z, Yu W, et al. Influence of erbium addition on the defects of selective laser-melted 7075 aluminium alloy. Virtual Phys Prototy. 2022;17(2):406–418. doi:10.1080/17452759.2021.1990358

[4] Banaee SA, Kapil A, Marefat F, et al. Generalised overlapping model for multi-material wire arc additive manufacturing (WAAM). Virtual Phys Prototy. 2023;18(1):e2210541. doi:10.1080/17452759.2023.2210541

[5] Xu R, Li R, Yuan T, et al. Microstructure, metallurgical defects and hardness of Al–Cu–Mg–Li–Zr alloy additively manufactured by selective laser melting. J Alloy Comp. 2020;835:155372. doi:10.1016/j.jallcom.2020.155372

[6] Jiao S, Cheng X, Shen S, et al. Microstructure evolution and mechanical behavior of Al–Li alloy fabricated by laser melting deposition technique. J Alloy Comp. 2020;821:153125. doi:10.1016/j.jallcom.2019.153125

[7] Wang X, Liu D, Cheng X. Effect of heat treatment process on microstructures and mechanical properties of laser additive manufactured Al-Li alloys. Chin J Lasers. 2018;45(5):68–75. doi:10.3788/CJL201845.0502004

[8] Sun GQ, Zhao GP, Xiong LX, et al. Particle dispersion and mechanical properties enhancement of in-situ TiB_2/7050 Al matrix composite via additive friction stir deposition. Mater Lett. 2024;357:135790. doi:10.1016/j.matlet.2023.135790

[9] Metz CP, Franz C, Kincaid J, et al. Heterogeneous microstructure development in additive friction-stir deposited Al-Mg-Si alloy. Addit Manuf. 2024;81:103989. doi:10.1016/j.addma.2024.103989

[10] Li Y, Zhang M, Wang H, et al. Microstructure and mechanical properties of Al–Li alloy manufactured by additive friction stir deposition. Mater Sci Eng A. 2023;887:145753. doi:10.1016/j.msea.2023.145753

[11] Zhao Z, Yang X, Li S, et al. Interfacial bonding features of friction stir additive manufactured build for 2195-T8 aluminum-lithium alloy. J Manuf Process. 2019;38:396–410. doi:10.1016/j.jmapro.2019.01.042

[12] Zhong H, Qi B, Cong B, et al. Microstructure and mechanical properties of wire + arc additively manufactured 2050 Al–Li alloy wall deposits. Chin J Mech Eng. 2019;32(1):1–7. doi:10.1186/s10033-019-0405-z

[13] Xue C, Zhang Y, Mao P, et al. Improving mechanical properties of wire arc additively manufactured AA2196 Al–Li alloy by controlling solidification defects. Addit Manuf. 2021;43:102019. doi:10.1016/j.addma.2021.102019

[14] Xiao Z, Yu W, Fu H, et al. Recent progress on microstructure manipulation of aluminium alloys manufactured via laser powder bed fusion. Virtual Phys Prototy. 2023;18(1):e2125880. doi:10.1080/17452759.2022.2125880

[15] Gu J, Ding J, Williams SW, et al. The strengthening effect of inter-layer cold working and post-deposition heat treatment on the additively manufactured Al 6.3Cu alloy. Mater Sci Eng A. 2016;651:18–26. doi:10.1016/j.msea.2015.10.101

[16] Qi Z, Cong B, Sun H, et al. Microstructure and mechanical properties of double-wire + arc additively manufactured Al-Cu-Mg alloys. J Mater Process Techn. 2018;255:347–353. doi:10.1016/J.JMATPROTEC.2017.12.019

[17] Yu Z, Yuan T, Xu M, et al. Microstructure and mechanical properties of Al-Zn-Mg-Cu alloy fabricated by wire + arc additive manufacturing. J Manuf Process. 2021;62:430–439. doi:10.1016/j.jmapro.2020.12.045

[18] Wang L, Wu T, Wang D, et al. A novel heterogeneous multi-wire indirect arc directed energy deposition for in-situ synthesis Al-Zn-Mg-Cu alloy: process, microstructure and mechanical properties. Addit Manuf. 2023;72:103639. doi:10.1016/j.addma.2023.103639

[19] Parwez MP, Sinha A N. Fabrication of third generation Al-Li alloy by friction stir welding: a review. Sādhanā. 2019;44(6):153. doi: 10.1007/s12046-019-1139-4

[20] Liu G, Xiong J, Tang L. Microstructure and mechanical properties of 2219 aluminum alloy fabricated by double-electrode gas metal arc additive manufacturing. Addit Manuf. 2020;35:101375. doi:10.1016/j.addma.2020.101375

[21] Li S, Zhang LJ, Ning J, et al. Microstructures and mechanical properties of Al–Zn–Mg aluminium alloy samples produced by wire + arc additive manufacturing. J Mater Res Technol. 2020;9(6):13770–13780. doi:10.1016/j.jmrt.2020.09.114

[22] Dong B, Cai X, Lin S, et al. Wire arc additive manufacturing of Al-Zn-Mg-Cu alloy: microstructures and mechanical properties. Addit Manuf. 2020;36:101447. doi:10.1016/j.addma.2020.101447

[23] Mcnamara K, Ji Y, Lia F, et al. Predicting phase transformation kinetics during metal additive manufacturing using non-isothermal Johnson-Mehl-Avrami models: application to Inconel 718 and Ti-6Al-4V. Addit Manuf. 2022;49:102478. doi:10.1016/j.addma.2021.102478

[24] Hu G, Cai X, Rong Y. *Fundamentals of materials science*. Shanghai: Shanghai Jiaotong University Press; 2010.

[25] Zeng CY, Sun XJ, Qi BJ, et al. In-situ TiC particles reinforced Al-6.3Cu alloy joint via ultrasonic frequency double-pulsed arc. Mater Sci Eng A. 2022;842:143078. doi:10.1016/j.msea.2022.143078

[26] Tong DL, Yi YP, He HL. Dynamic recrystallization and crystal phase evolution and its influence on static recrystallization and three-dimensional mechanical properties

of the multi-directionally forged 2195 Al-Li alloy. Mater. Sci. Eng. A., 2025;923:147707–147707. dol: 10.1016/J.MSEA.2024.147707

[27] Zhang SF, Zeng WD, Yang WH, et al. Ageing response of a Al-Cu-Li 2198 alloy. Mater Des. 2014;63:368–374. doi:10.1016/j.matdes.2014.04.063

[28] Liu D, Wu D, Ge C, et al. Superior strength of laser-arc hybrid additive manufactured Al-Zn-Mg-Cu alloy enabled by a tunable microstructure. Addit Manuf. 2023;68:103526. doi:10.1016/j.addma.2023.103526

[29] Li Q, Li G, Lin X, et al. Development of a high strength Zr/Sc/Hf-modified Al-Mn-Mg alloy using laser powder bed fusion: design of a heterogeneous microstructure incorporating synergistic multiple strengthening mechanisms. Addit Manuf. 2022;57:102967. doi:10.1016/j.addma.2022.102967

[30] Liu D, Wu D, Ma G, et al. Effect of post-deposition heat treatment on laser-TIG hybrid additive manufactured Al-Cu alloy. Virtual Phys Prototy. 2020;15:445–459. doi:10.1080/17452759.2020.1818021

[31] Ma K, Wen H, Tao H H, et al. Mechanical behavior and strengthening mechanisms in ultrafine grain precipitation-strengthened aluminum alloy. Acta Mater. 2014;62:141–155. doi:10.1016/j.actamat.2013.09.042

[32] Dixit M, Mishra RS, Sankaran KK. Structure-property correlations in Al 7050 and Al 7055 high-strength aluminum alloys. Mater Sci Eng A. 2007;478:163–172. doi:10.1016/j.msea.2007.05.116

[33] Yu W, Wang Y, Li Y, et al. Texture evolution, segregation behavior, and mechanical properties of 2060 Al-Li (aluminium-lithium) composites reinforced by TiC (titanium carbide) nanoparticles. Compos Part B Eng. 2023;255:110611. doi:10.1016/j.compositesb.2023.110611

[34] Dai W, Jiang Y, Yao JG, et al. Simultaneously improving the strength and ductility of an Ag-free 2195Al-Li alloy by T8 treatment with cryogenic pre-rolling. J Alloy Comp. 2024;976:173214. doi:10.1016/j.jallcom.2023.173214

[35] Chen X, Ma X, Zhao G, et al. Effects of re-solution and re-aging treatment on mechanical property, corrosion resistance and electrochemical behavior of 2196 Al-Cu-Li alloy. Mater Design. 2021;204:109662. doi:10.1016/j.matdes.2021.109662

[36] Li H, Zou Z, Li J, et al. Correlation between grain structures and tensile properties of Al-Li alloys. Trans Nonferrous Met Soc China. 2023;12:3597. doi:10.1016/S1003-6326(23)66357-5

[37] Wang L, Hu H, Wu T, et al. Effect of alloying powders on microstructure and mechanical properties of aluminum alloy arc additive manufacturing, 3D print. Addit Manuf. 2023;10(1):83–100. doi:10.1089/3dp.2021.0055